Supplementary Information

High-Efficiency White Hyperfluorescence Based on TADF Sensitizer Matrixes *via* Spatial and Energy Gap Effects

*Chunbo Duan, Ying Xin, Zicheng Wang, Jing Zhang, Chunmiao Han and Hui Xu**

Key Laboratory of Functional Inorganic Material Chemistry, Ministry of Education & School of Chemistry and Material Science, Heilongjiang University

74 Xuefu Road, Harbin 150080, P. R. China

*Corresponding author.

E-mail: hxu@hlju.edu.cn

Content

I. Experimental section (Scheme S1)

1. Materials and Instruments

Chemical Structure Characteristics. ^{1}H NMR spectra were recorded using a Varian Mercury plus 400NB spectrometer relative to tetramethylsilane (TMS) as internal standard. Molecular masses were determined by electrospray ionization mass spectrometry or matrix-assisted laser desorption/ionization mass spectrometry using a Finnigan LCQ instrument. Elemental analyses were performed on a Vario EL III elemental analyzer. The crystals suitable for single-crystal XRD analysis was obtained through slowly diffusing hexane into dichloromethane solutions of the materials at room temperature. All diffraction data were collected at 295 K on a Rigaku Xcalibur E diffractometer with graphite monochromatized Mo Kα (λ = 0.71073 Å) radiation in ω scan mode. All structures were solved by direct method and difference Fourier syntheses. Non-hydrogen atoms were refined by full-matrix least-squares techniques on F2 with anisotropic thermal parameters. The hydrogen atoms attached to carbons were placed in calculated positions with C−H = 0.93 Å and U(H) = 1.2Ueq(C) in the riding model approximation. All calculations were carried out with the SHELXL97 program.

Thermal Analysis. Thermogravimetric analysis (TGA) and differential scanning calorimetry (DSC) were performed on Shimadzu DSC-60A and DTG-60A thermal analyzers under a nitrogen atmosphere at a heating rate of 10 ℃ min^{-1}.

Electrochemical Characteristics. Cyclic voltammetry (CV) studies were conducted using an Eco Chemie B.V. AUTOLAB potentiostat in a typical three-electrode cell with a glassy carbon working electrode, a platinum wire counter electrode, and a silver/silver chloride reference electrode. All electrochemical experiments were carried out under a nitrogen atmosphere at room temperature in dichloromethane and tetrahydrofuran respectively for oxidation and reduction.

Photophysical Measurement. Absorption spectra were measured using a Shimadzu UV-3150 spectrophotometer. Steady-state and time-resolved emission spectra were

measured with an Edinburgh FPLS 1000 fluorescence spectrophotometer. Phosphorescence spectra were recorded at 77 K, cooled by liquid nitrogen, after a delay of 300 μs using a time-correlated single photon counting method with a microsecond pulsed xenon light source for 0.1 μs−10 s lifetime measurement, which was also used to measure time decays of delayed fluorescence (DF). Another nanosecond pulsed hydrogen lamp for 0.1 ns−10 μs measurement was used to record time decays of prompt fluorescence (PF). Data were processed with the synchronization photomultiplier for signal collection, and the multi-channel scaling mode of the PCS900 fast counter PC plug-in card. The variable-temperature transient emission decay spectra were measured with a temperature controller over a range of 11−500 K. All the films were prepared by vacuum evaporation for optical analysis. PLQYs (ϕ_{PL}) of these films were measured through a Labsphere 1-M-2 integrating sphere (ϕ = 6 in.) coated with Benflect material with efficient light reflection in a wide range of 200−1600 nm, which was integrated with an FPLS 920 fluorescence spectrophotometer. The absolute η_{PL} of the sample was determined by performing two spectral (emission) scans, with the emission monochromator scanning over the Rayleigh scattered light from the sample and from a blank substrate. The first spectrum recorded the scattered light and the emission of the sample, and the second spectrum recorded the scattered light of the Benflect coating. Integration and subtraction of the scattered light parts of these two spectra provided the photon number absorbed by the samples (*N*a), while integration of the emission of the samples was done to calculate the emissive photon number (*N*e). The absolute ϕ_{PL} can then be estimated according to the equation $\phi_{PL} = Ne/Na$. Spectral correction (emission arm) was applied to the raw data after background subtraction, and from these spectrally corrected curves, the quantum yield was calculated using aF900 software wizard.

2. Synthesis

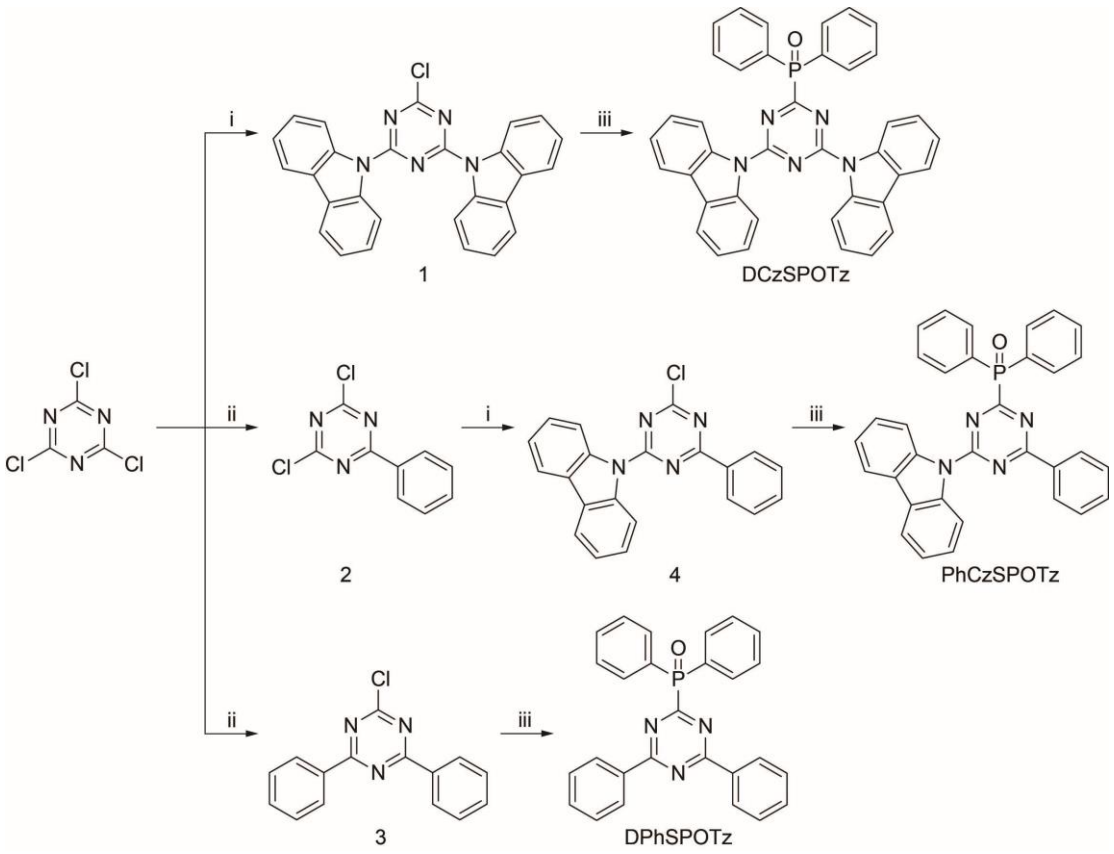

Scheme S1. Synthetic procedures of DCzSPOTz, PhCzSPOTz and DPhSPOTz: i. carbazole, *n*-BuLi, THF, 0 ^{o}C/4 h to r.t./8 h; ii. bromobenzene, Mg, THF, 60 ^{o}C/1h to r.t./12 h; iii. Ph_2PH, DMF, 100 ^{o}C, 24 h; 30% H_2O_2, 0 ^{o}C, 3 h.

9,9'-(6-Chloro-1,3,5-triazine-2,4-diyl)bis(9H-carbazole) (1)*:* In N_2, *n*-BuLi (2.5 M in *n*-hexane, 6 mL, 15 mmol) was added dropwise to tetrahydrogenfuran (THF) solution (20 mL) of carbazole (2.0 g, 12 mmol) at 0 ^{o}C. The reaction was stirred for 4 h, and then the mixture was added dropwise into THF solution (15 mL) of 2,4,6-trichloro-1,3,5-triazine (0.9 g, 5 mmol) at room temperature. After stirring for 8 h, the reaction was quenched by 50 mL of water. The reaction was extracted by dichloromethane (DCM, 3×10 mL). The organic layer was combined and dried with anhydrous Na_2SO_4. The solvent was removed by rotary evaporation, and the residue was purified by flash column chromatography to afford **1** as white powder with a high yield of 70%.

^{1}H NMR (TMS, $CDCl_3$, 400 MHz): δ = 8.863 (d, J = 8.4 Hz, 4H), 7.991 (d, J = 7.2 Hz, 4H), 7.544 (t, J = 7.8 Hz, 4H), 7.454 ppm (t, J = 7.8 Hz, 4H); LDI-MS: m/z (%):

445 (100) [M^+]; elemental analysis (%) for $C_{27}H_{16}ClN_5$: C 72.73, H 3.62, N 7.95; found: C 72.72, H 3.64, N 7.97.

Gernal procedure of phenylation reaction*:* In N_2, bromobenzene (1.1 mL, 10.5 mmol) in 15 mL of THF was added dropwise into a mixture of Magnesium turning (0.29 g, 12 mmol) and a small piece of I_2 in 5 mL THF at room temperature. The reaction was stirred at 60 ^oC for 1 h. Then, the generated Grignard reagent was added dropwise in the mixture of 2,4,6-trichloro-1,3,5-triazine (1.8 g, 10 mmol for **2** or 0.9 g, 5 mmol for **3**) in 10 mL of THF at 0 ^oC (for **2**) or room temperature (for **3**). After stirring for 12 h, the reaction was quenched by 50 mL of water and extracted with dichloromethane (3×20 mL). The organic layer was combined and dried with anhydrous Na_2SO_4. The solvent was removed by rotary evaporation and the residue was purified by column chromatography to afford **2** and **3** as white powders respectively with yields of 60% and 45 %.

2,4-Dichloro-6-phenyl-1,3,5-triazine (2): ^{1}H NMR (TMS, $CDCl_3$, 400 MHz): δ = 8.503 (d, J = 7.6 Hz, 2H); 7.661 (t, J = 7.4 Hz, 1H); 7.537 ppm (t, J = 7.8 Hz, 2H); LDI-MS: m/z (%): 225 (100) [M^+]; elemental analysis (%) for $C_9H_5Cl_2N_3$: C 47.82, H 2.23, N 18.59; found: C 47.84, H 2.22, N 18.51.

2-Chloro-4,6-diphenyl-1,3,5-triazine (3): ^{1}H NMR (TMS, $CDCl_3$, 400 MHz): δ = 8.622 (d, J = 7.2 Hz, 4H); 7.635 (t, J = 7.2 Hz, 2H); 7.553 ppm (t, J = 7.6 Hz, 4H); LDI-MS: m/z (%): 269 (100) [M^+]; elemental analysis (%) for $C_{15}H_{10}ClN_3$: C 67.30, H 3.77, N 15.70; found: C 67.31, H 3.78, N 15.72.

9-(4-Chloro-6-phenyl-1,3,5-triazin-2-yl)-9H-carbazole (4): The procedure similar to **1** was adopted to synthesize **4** from **2**, affording to **4** as white powder with a yield of 60%.

^{1}H NMR (TMS, $CDCl_3$, 400 MHz): δ = 9.028 (d, J = 8.4 Hz, 2H); 8.598 (d, J = 7.2 Hz, 2H); 8.037 (d, J = 7.6 Hz, 2H); 7.677 (t, J = 7.2 Hz, 1H); 7.586 (dd, J_1 = 8.0 Hz, J_2 = 6.6 Hz, 4H); 7.452 ppm (t, J = 7.2 Hz, 2H); LDI-MS: m/z (%): 356 (100) [M^+];elemental analysis (%) for $C_{21}H_{13}ClN_4$: C 70.69, H 3.67, N 15.70; found: C 70.68, H 3.68, N 15.72.

3. DFT Calculations

DFT computations were carried out with different parameters for structure optimizations and vibration analyses. The ground state configurations were optimized by the restricted and unrestricted formalism of Beck's three-parameter hybrid exchange functional[1] and Lee, and Yang and Parr correlation functional[2] B3LYP/6-31G(d,p), respectively. The fully optimized stationary points were further characterized by harmonic vibrational frequency analysis to ensure that real local minima had been found without imaginary vibrational frequency. The total energies were also corrected by zero-point energy both for the ground state and triplet state. Natural transition orbital (NTO) analysis was performed on the basis of optimized ground-state geometries at the level of B3LYP/6-31G(d,p).[3] The contours were visualized with Gaussview 5.0. All computations were performed using the Gaussian 09 package.[4]

4. Parameter Estimation of PF and DF

The quantum efficiencies (η_{PF}, η_{DF}, η_{DF} and) and constants (k_{PF} and k_{DF}) of PF and DF can be estimated according to their contributions to total ϕ_{PL} and their lifetimes (τ_{PF} and τ_{DF}) according to transient emission spectra. The PF and DF components (I_{PF} and I_{DF}) are roughly estimated by the time range before and after 1 μs, respectively. The parameters can be calculated according to

$$k_{PF} = k_r^S + k_{nr}^S + k_{ISC} \quad \text{Eq. S1}$$

$$k_{DF} = k_{nr}^T + \left(1 - \frac{k_{ISC}}{k_{PF}}\right) \cdot k_{RISC} \quad \text{Eq. S2}$$

$$k_r^S = \eta_{PF} \cdot k_{PF} \quad \text{Eq. S3}$$

$$k_{nr}^S = k_{PF} - k_r^S - k_{ISC} = k_{PF} - k_r^S - k_{PF} \cdot \frac{\eta_{PF}}{\eta_{PL}} \quad \text{Eq. S4}$$

$$k_{nr}^T = k_{DF} - \left(1 - \frac{k_{ISC}}{k_{PF}}\right) \cdot k_{RISC} = k_{DF} - \left(1 - \frac{k_{ISC}}{k_{PF}}\right) \cdot \frac{k_{DF} \cdot k_{PF} \cdot \eta_{DF}}{k_{ISC} \cdot \eta_{PF}} \quad \text{Eq. S5}$$

$$\eta_{ISC} = \frac{k_{ISC}}{k_{PF}} \quad \text{Eq. S6}$$

$$\eta_{RISC} = \frac{k_{RISC}}{k_{RISC}+k_{nr}^{T}} \quad \text{Eq. S7}$$

5. Fabrication and Characterization of OLEDs

Before loading into a deposition chamber, the ITO substrate was cleaned with detergents and deionized water, dried in an oven at 120 ℃ for 4 h, and treated with UV-ozone for 20 min. Devices were fabricated by evaporating organic layers at a rate of 0.1-0.3 nm s^{-1} onto the ITO substrate sequentially at a pressure below 1×10^{-6} mbar. Onto the electron transporting layer, a layer of LiF with 1 nm thickness was deposited at a rate of 0.1 nm s^{-1} to improve electron injection. Finally, a 100-nm-thick layer of Al was deposited at a rate of 0.6 nm s^{-1} as the cathode. The emission area of the devices was 0.09 cm^2 as determined by the overlap area of the anode and the cathode. The EL spectra and CIE coordinates were measured using a PR655 spectra colorimeter. The current-density-voltage and brightness–voltage curves of the devices were measured using a Keithley 4200 source meter and a calibrated silicon photodiode. All the measurements were carried out at room temperature in glove box. For each structure, four devices were fabricated in parallel to confirm the performance repeatability. EL transient spectra were measured with Edinburgh FLS1000 equipped with a Tektronix AFG3022G function generator. The driving voltage was 5 V. The pulse width was 20 μs.

The blue and yellow components from TBPe and TBRb to white emissions were estimated with dual-peak fitting. The contributions of blue and yellow components to total white emissions were evaluated with the ratios of blue and yellow peak areas to total emission areas, which were further used to calculate blue and yellow η_{EQE} from total η_{EQE}.

II. Single Crystal Results (Fig S1)

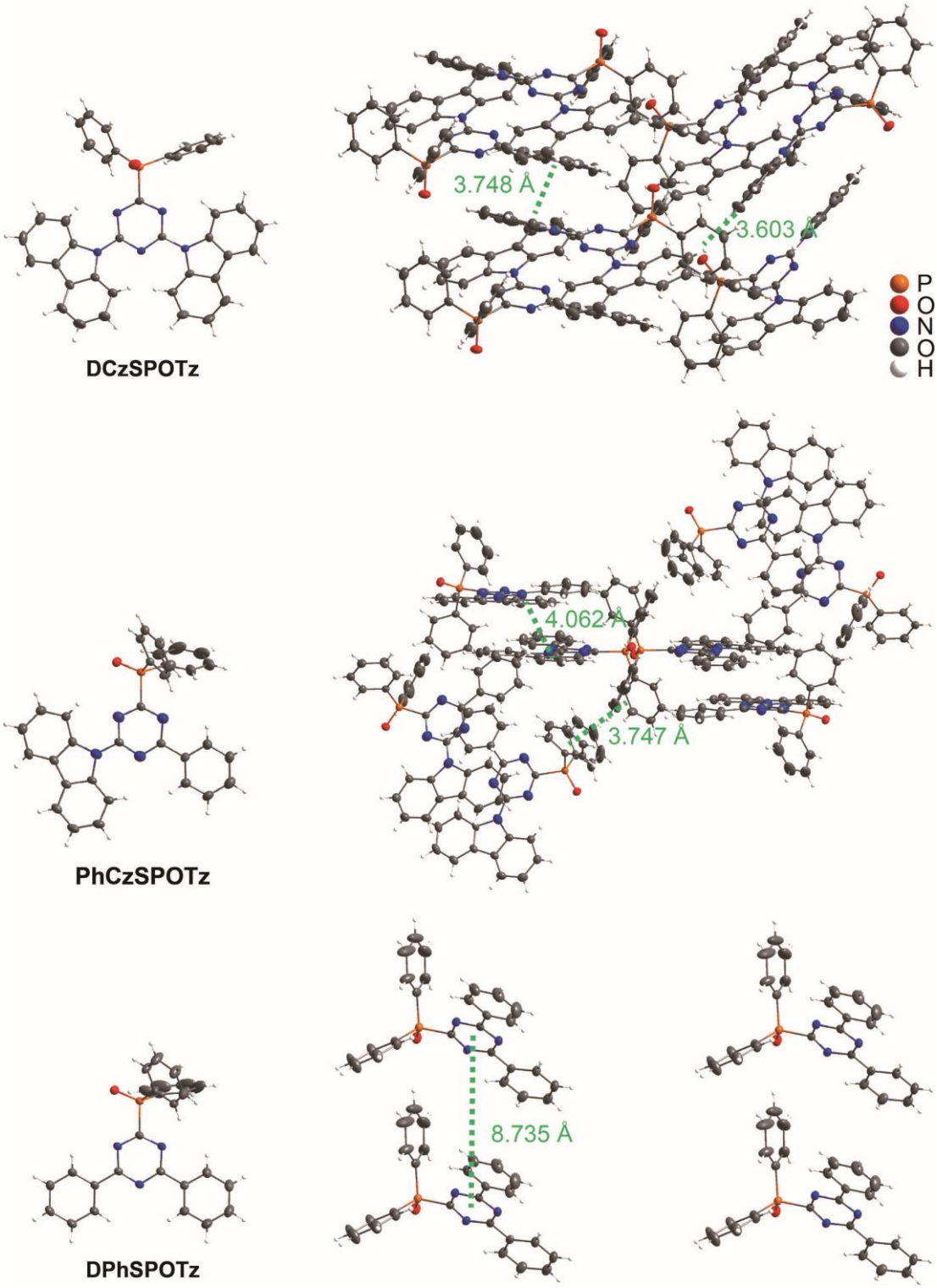

Figure S1. Single crystal structures and packing diagrams of DCzSPOTz, PhCzSPOTz and DPhSPOTz.

The single crystal packing diagram of DCzSPOTz reveals relatively stronger intermolecular π-π stacking interactions between adjacent Cz groups with a centroid-centroid distance of 3.7 Å, and Cz and DPPO groups with a centroid-edge distance of 3.6 Å, respectively (**Figure S1**). On the contrary, in DPhSPOTz, large volume proportion of DPPO amplifies its steric effect on interaction suppression, inducing markedly elongated intermolecular distance of 8.7 Å. The asymmetric configuration of PhCzSPOTz induces the stagger between Cz groups in adjacent molecules with centroid distance beyond 4 Å, basically excluding π-π stacking interactions. However, weak intermolecular interactions between DPPO groups with centroid-edge distances of 3.7 Å still exist, supporting sufficient electron transportation.

III. Thermal Properties (Fig S2)

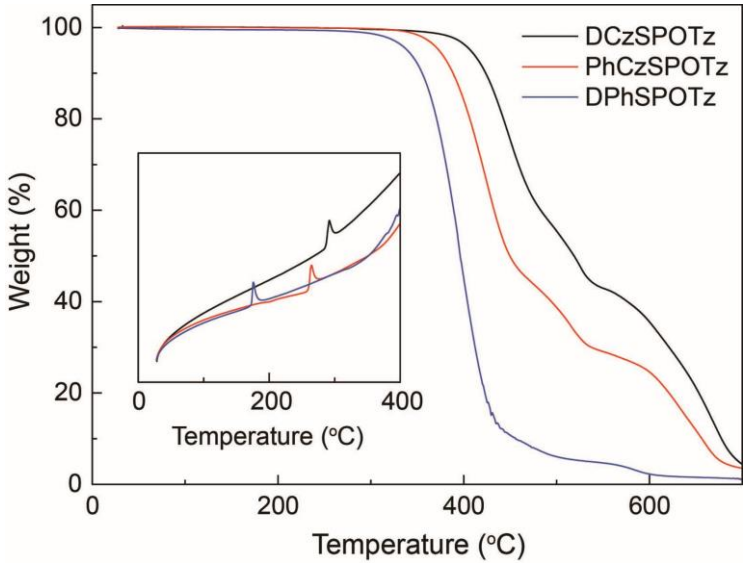

Figure S2. Thermogravimetric analysis (TGA) and differential scanning calorimetry (DSC) curves of DCzSPOTz, PhCzSPOTz and DPhSPOTz.

IV. Solvatochromic Properties (Fig S3 and Table S1)

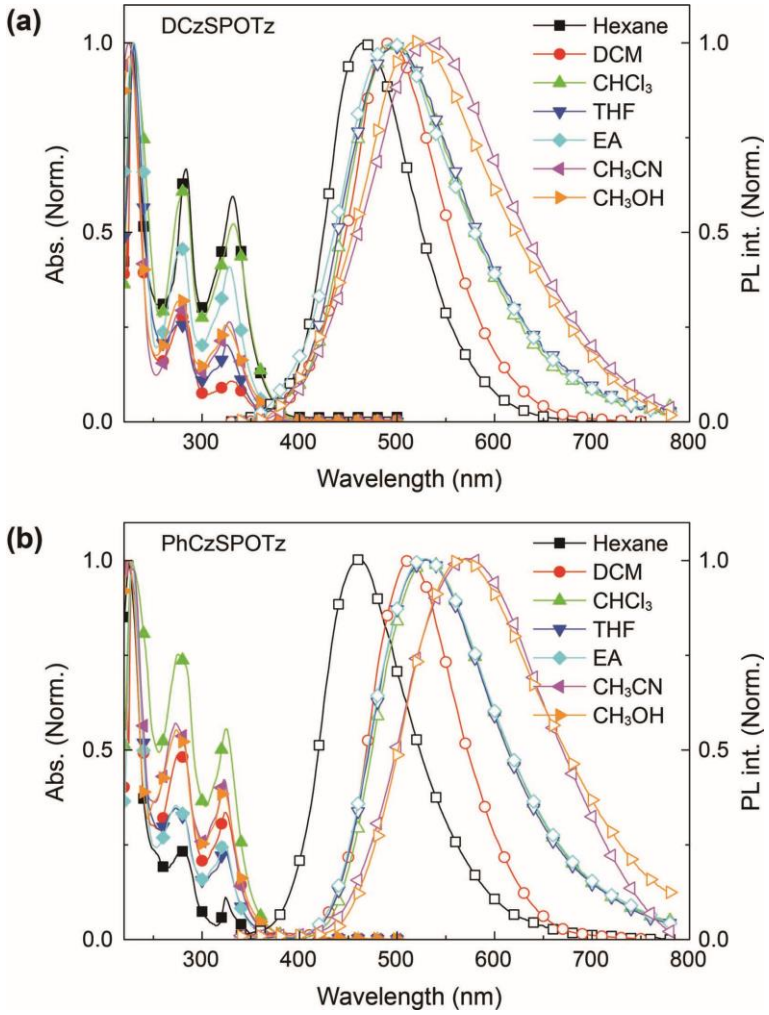

Figure S3. Absorption and emission spectra of DCzSPOTz, PhCzSPOTz and DPhSPOTz in different solvents with various polarities (10^{-5} M).

Table S1. Physical properties of DCzSPOTz, PhCzSPOTz and DPhSPOTz.

TADF host	$\lambda_{Abs.}$ (nm)	λ_{PL} (nm)	S_1 (eV)	T_1 (eV)	ΔE_{ST}[c] (eV)	Tm/T_d[d] (^oC)	HOMO[e] (eV)	LUMO[e] (eV)	f_s[f]
DCzSPOTz	331, 280, 228[a] 331, 281, 228[b]	494[a] 472[b]	3.14[d] 3.58[e]	3.02[f] 3.15[e]	0.12[a] 0.43[b]	291/407	- 6.33[g] -5.82[e]	-3.43[g] -1.64[e]	0.5797
PhCzSPOTz	324, 277, 228[a] 324, 381, 228[b]	512[a] 484[b]	3.04[d] 3.36[e]	3.04[f] 3.10[e]	0.00[a] 0.26[b]	266/373	-6.54[g] -5.80[e]	-3.42[g] -1.89[e]	0.81323
DPhSPOTz	277, 228 [a] 281, 227 [b]	406, 434[a] 404, 494[b]	3.54[d] 3.84[e]	3.08[f] 3.14[e]	0.46[a] 0.70[b]	175/339	-6.41[g] -5.81[e]	-3.28[g] -1.83[e]	0.7525

[a] In dichloromethane solution (10^{-5} mol L^{-1}); [b] in film; [c] singlet-triplet splitting; [d] melting point/decomposition temperature at weight loss of 5%; [e] calculated according to cyclic voltammetric results; [f] oscillator strength of $S_0 \rightarrow S_1$ transition estimated by absorption spectra in dichloromethane (10^{-5} mol L^{-1}).

V. Device Performance (Figs S4-S18 and Table S2)

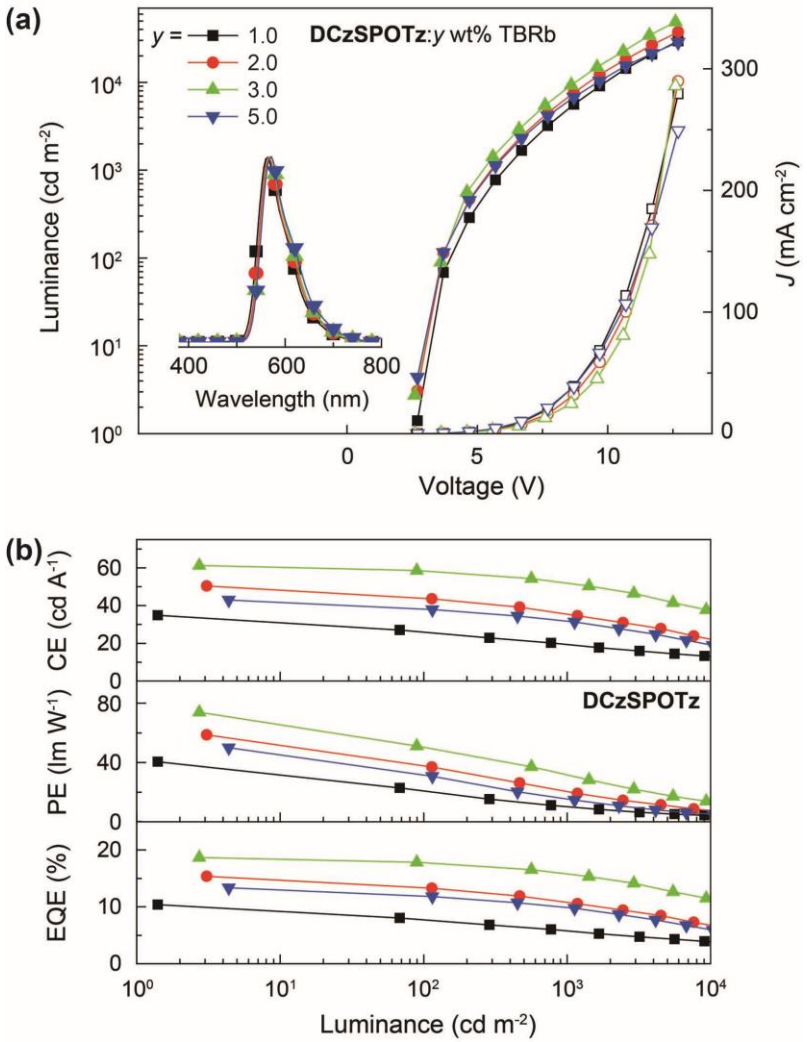

Figure S4. (a) Luminance-current density (*J*)-voltage curves and EL spectra (inset) of DCzSPOTz:*y* wt% TBRb-based devices with different TBRb concentration of 1.0, 2.0, 3.0 and 5.0 wt%; (b) efficiencies-luminance relationships of the devices.

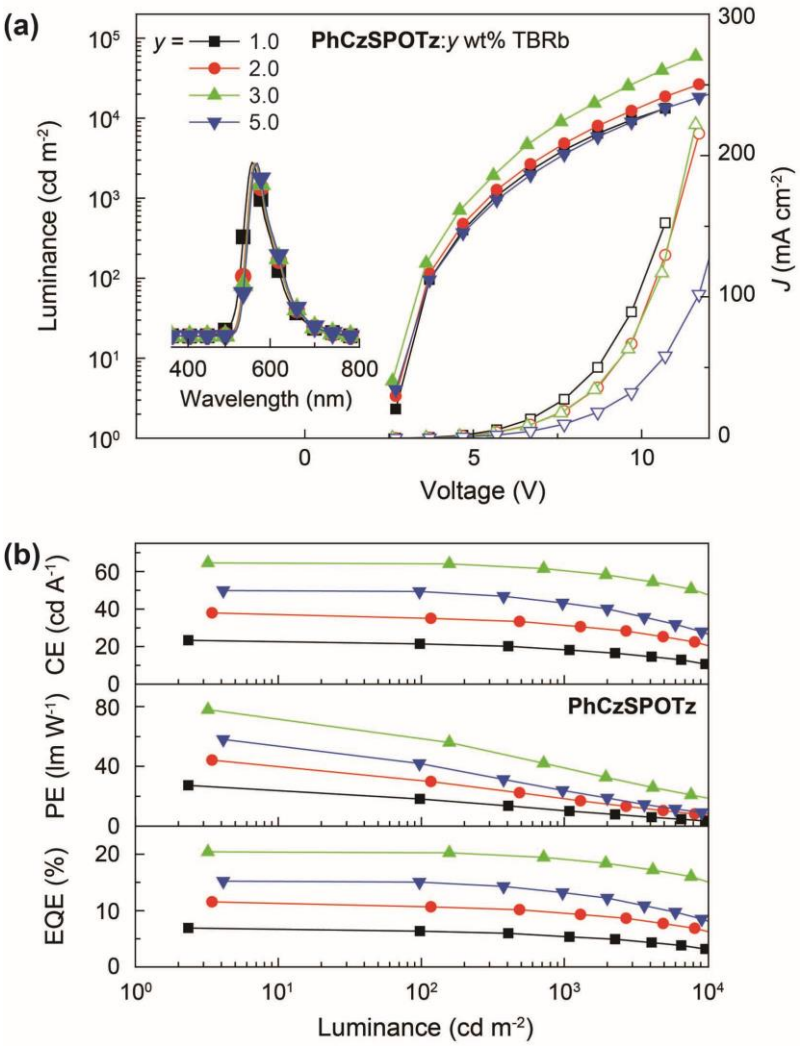

Figure S5. (a) Luminance-current density (*J*)-voltage curves and EL spectra (inset) of PhCzSPOTz:*y* wt% TBRb-based devices with different TBRb concentration of 1.0, 2.0, 3.0 and 5.0 wt%; (b) efficiencies-luminance relationships of the devices.

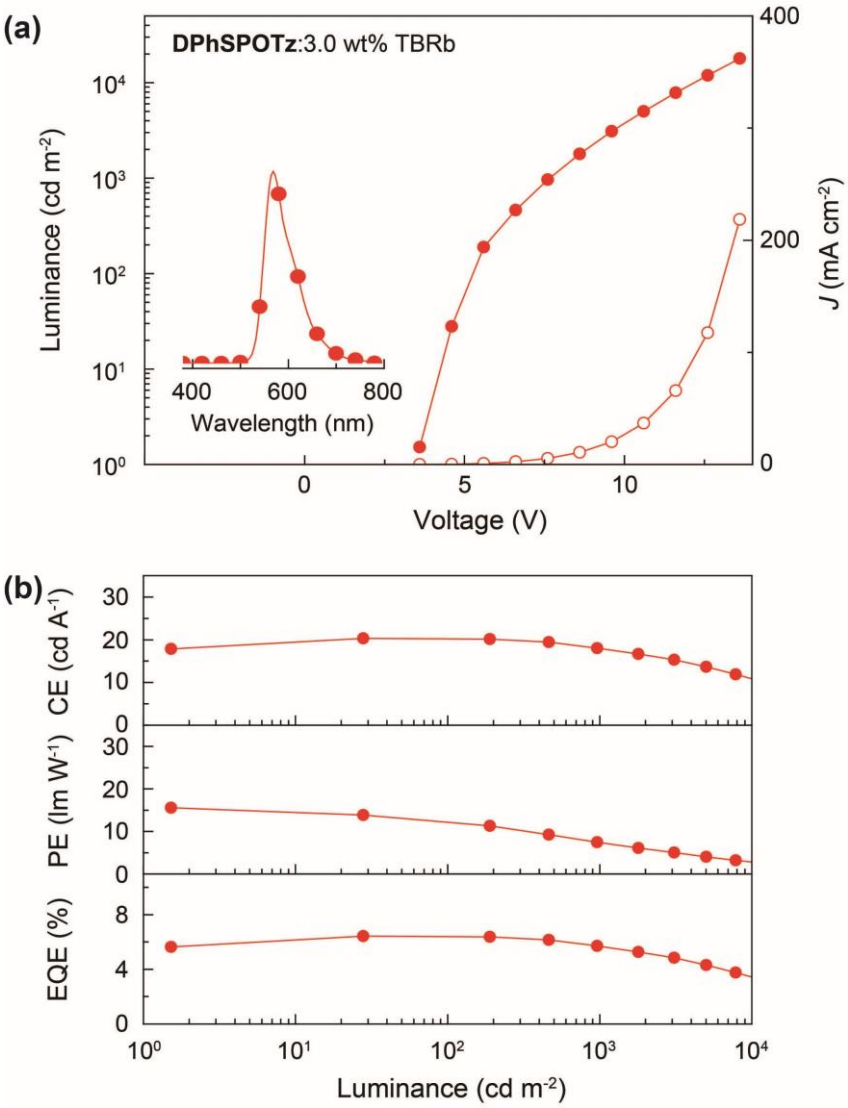

Figure S6. (a) Luminance-current density (*J*)-voltage curves and EL spectra (inset) of DPhSPOTz:3.0% TBRb-based devices; (b) efficiencies-luminance relationships of the devices.

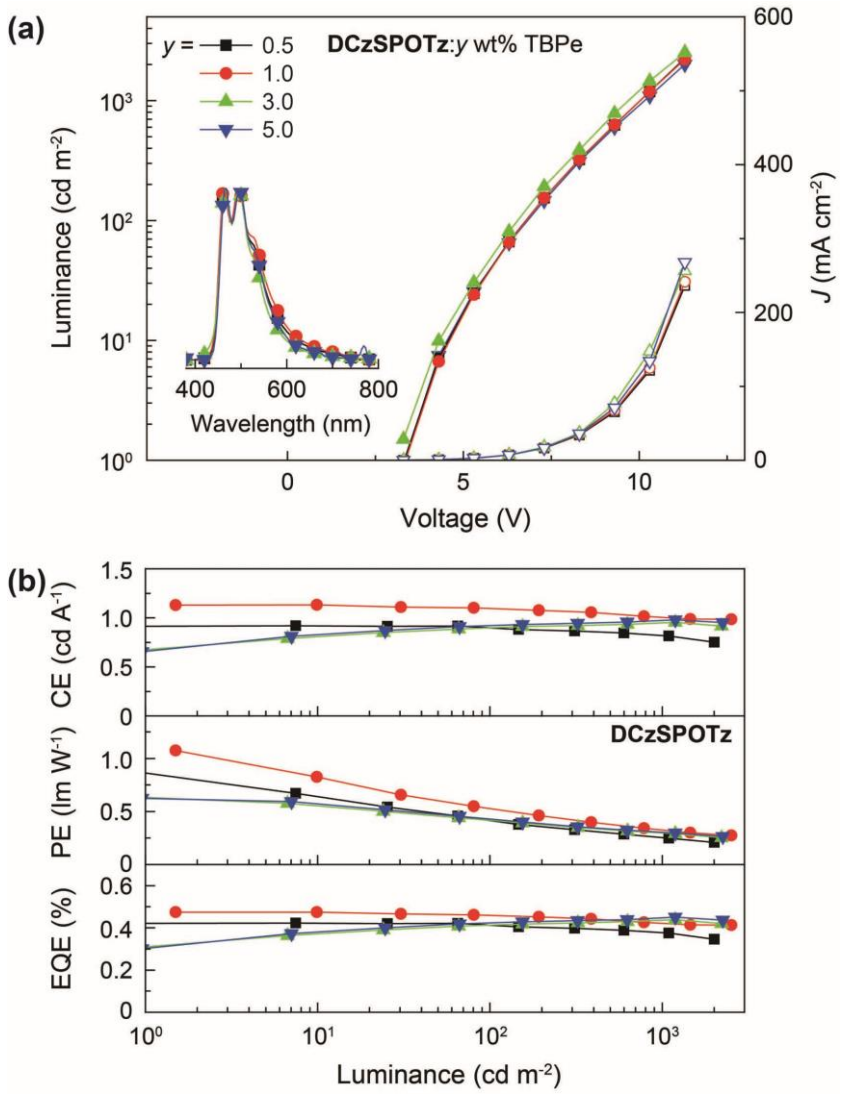

Figure S7. (a) Luminance-current density (*J*)-voltage curves and EL spectra (inset) of DCzSPOTz:*y* wt% TBPe-based devices with different TBPe concentration of 0.5, 1.0, 3.0 and 5.0 wt%; (b) efficiencies-luminance relationships of the devices.

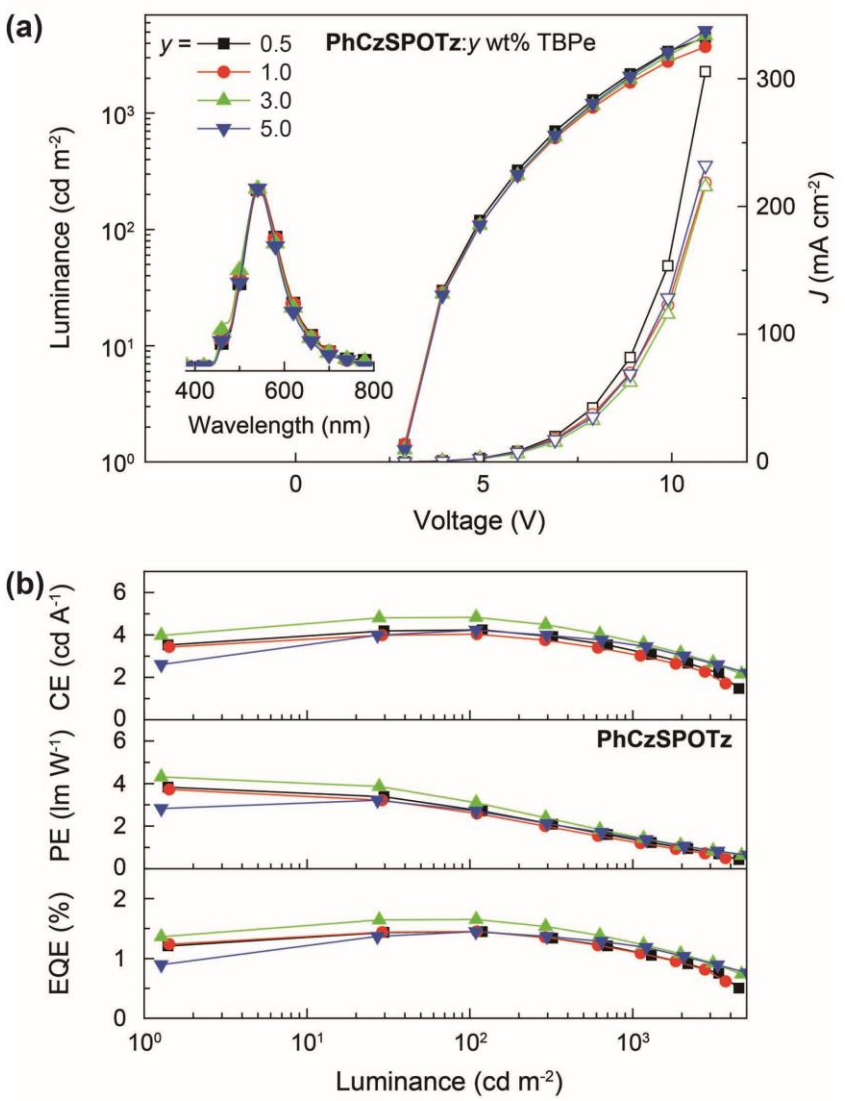

Figure S8. (a) Luminance-current density (*J*)-voltage curves and EL spectra (inset) of PhCzSPOTz:*y* wt% TBPe-based devices with different TBPe concentration of 0.5, 1.0, 3.0 and 5.0 wt%; (b) efficiencies-luminance relationships of the devices.

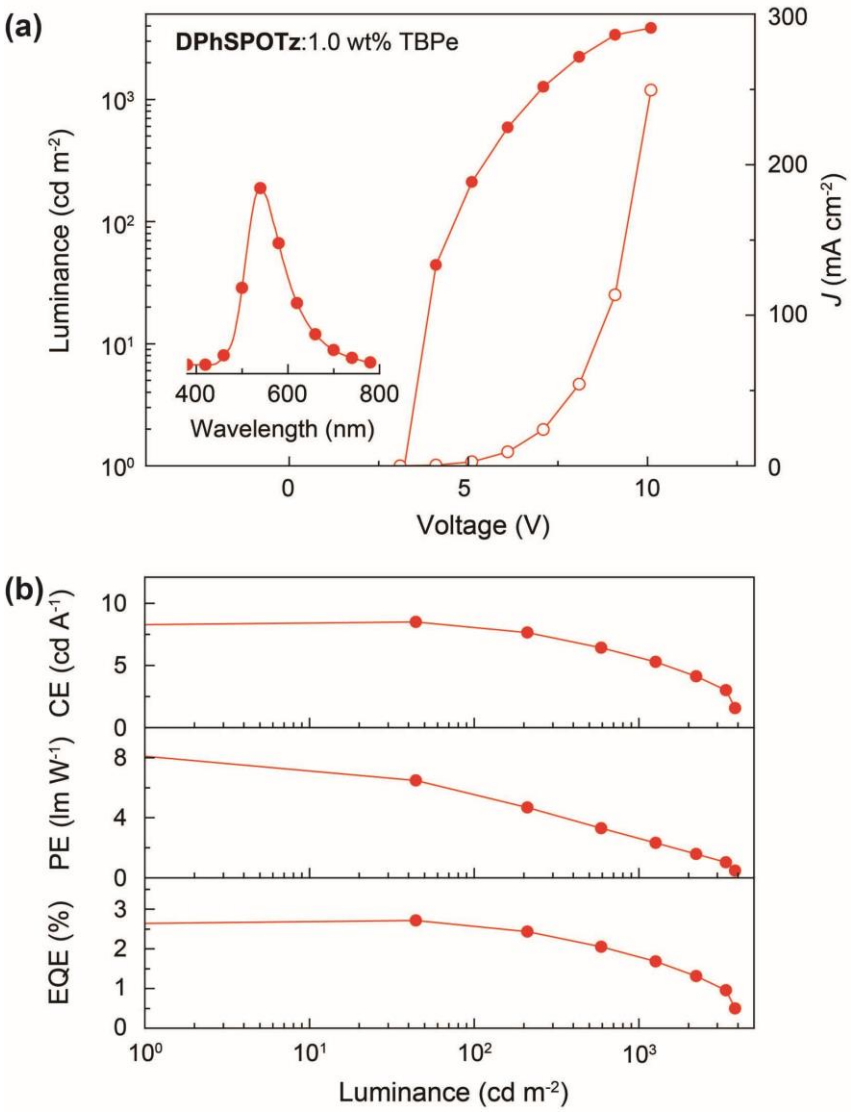

Figure S9. (a) Luminance-current density (*J*)-voltage curves and EL spectra (inset) of DPhSPOTz:1.0% TBPe-based devices; (b) efficiencies-luminance relationships of the devices.

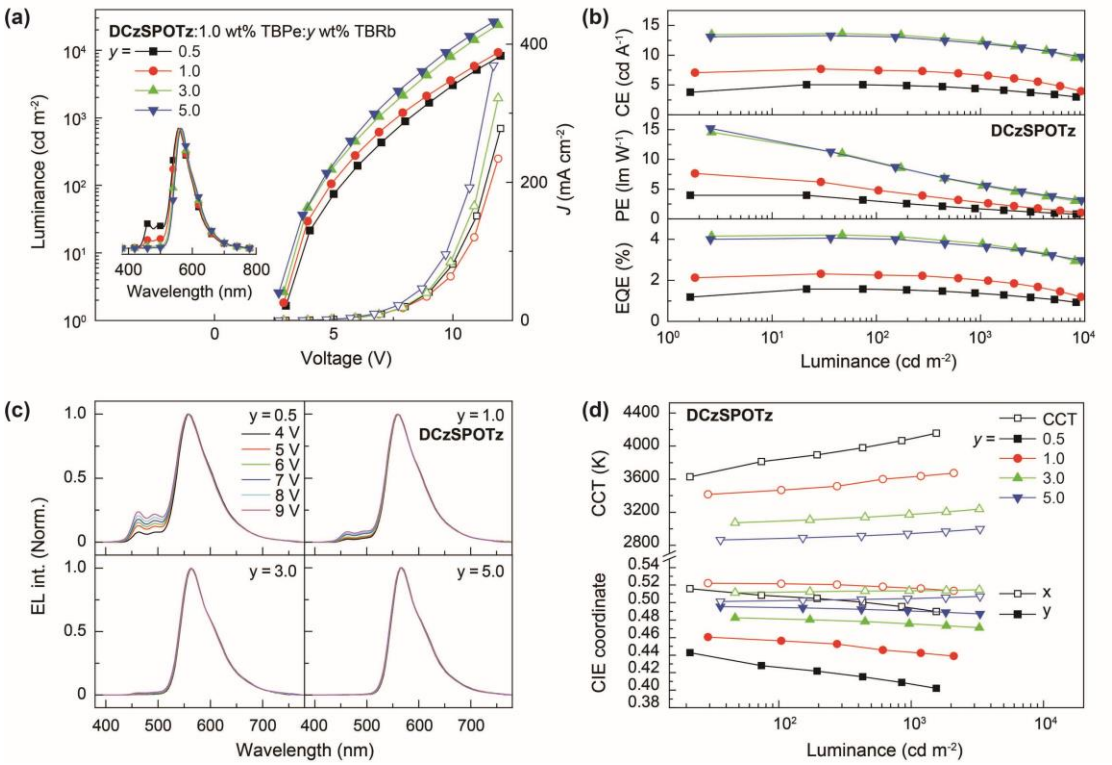

Figure S10. (a) Luminance-current density (*J*)-voltage curves and EL spectra (inset) of DCzSPOTz:1.0 wt% TBPe:*y* wt% TBRb-based dually doped *s*EML WOLEDs with different TBRb concentration of 0.5, 1.0, 3.0 and 5.0 wt%; (b) efficiencies-luminance relationships of the WOLEDs; (c) EL spectrum dependence of the WOLEDs at the voltage range of 4-9 V; (d) CIE coordination (x, y) and correlated color temperature (CCT) variations of the WOLEDs at different luminance.

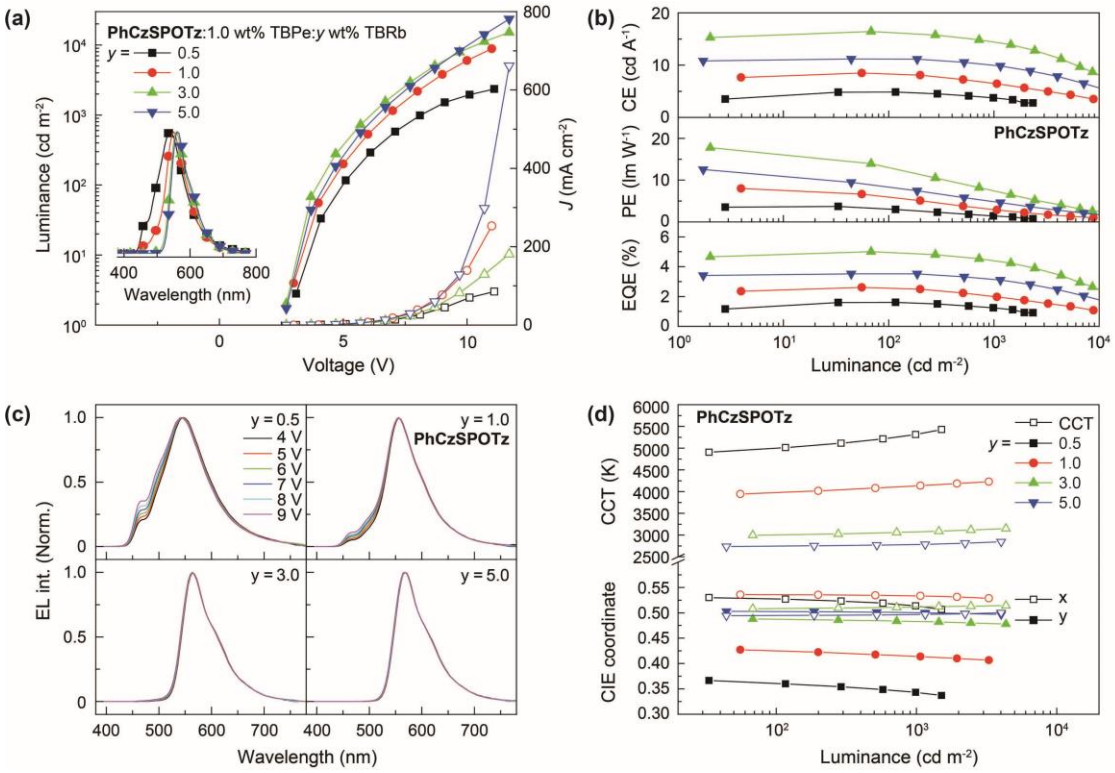

Figure S11. (a) Luminance-current density (*J*)-voltage curves and EL spectra (inset) of PhCzSPOTz:1.0 wt% TBPe:*y* wt% TBRb-based dually doped *s*EML WOLEDs with different TBRb concentration of 0.5, 1.0, 3.0 and 5.0 wt%; (b) efficiencies-luminance relationships of the WOLEDs; (c) EL spectrum dependence of the WOLEDs at the voltage range of 4-9 V; (d) CIE coordination (x, y) and correlated color temperature (CCT) variations of the WOLEDs at different luminance.

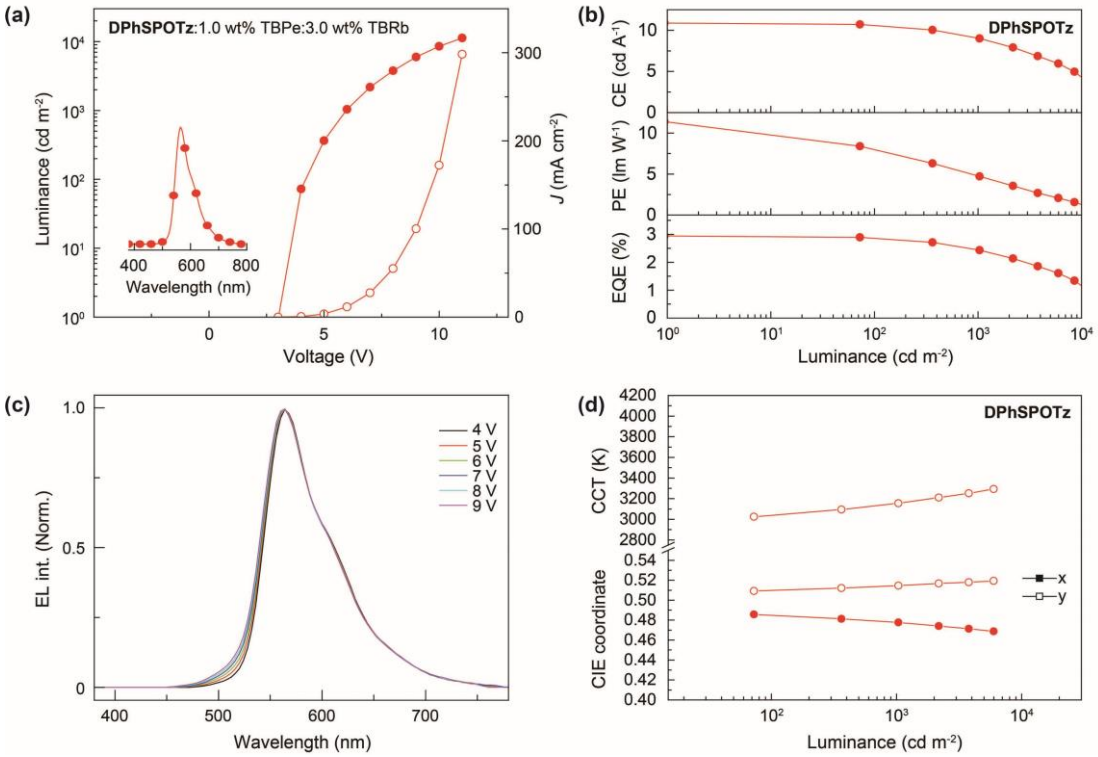

Figure S12. (a) Luminance-current density (*J*)-voltage curves and EL spectra (inset) of DPhSPOTz:1.0 wt% TBPe:3.0 wt% TBRb-based dually doped *s*EML WOLEDs; (b) efficiencies-luminance relationships of the WOLEDs; (c) EL spectrum dependence of the WOLEDs at the voltage range of 4-9 V; (d) CIE coordination (x, y) and correlated color temperature (CCT) variations of the WOLEDs at different luminance.

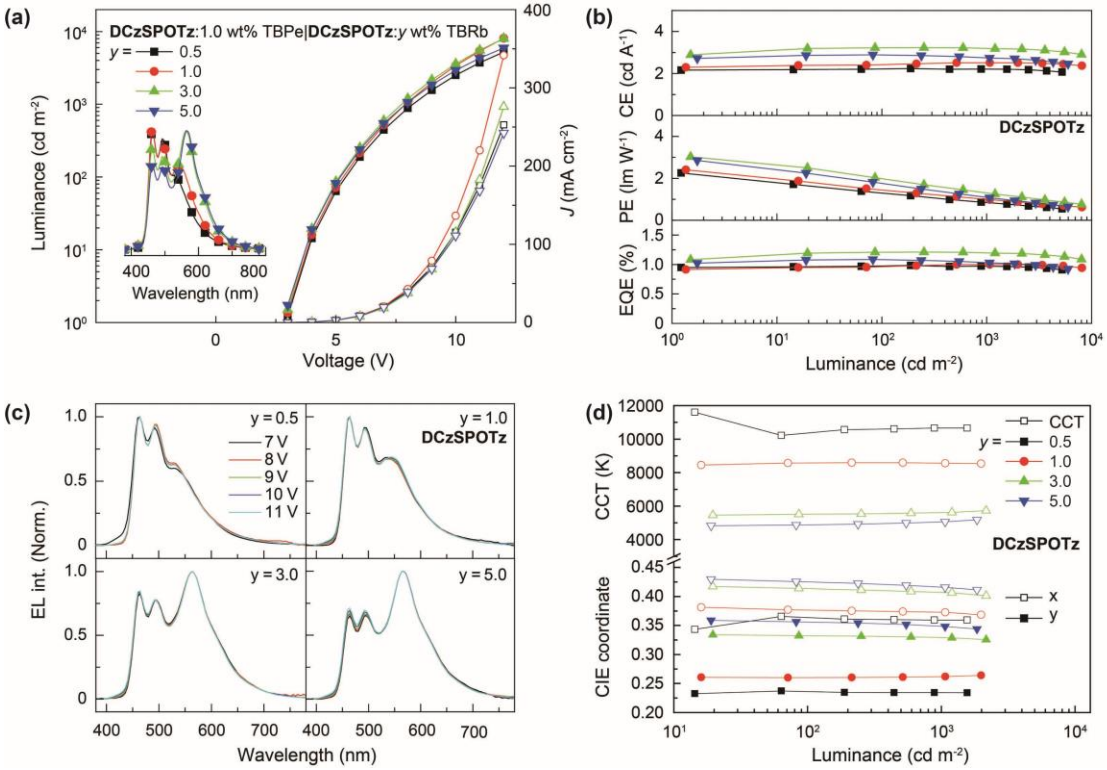

Figure S13. (a) Luminance-current density (*J*)-voltage curves and EL spectra (inset) of DCzSPOTz:1.0 wt% TBPe|DCzSPOTz:*y* wt% TBRb-based singly doped *d*EML WOLEDs with different TBRb concentration of 0.5, 1.0, 3.0 and 5.0 wt%; (b) efficiencies-luminance relationships of the WOLEDs; (c) EL spectrum dependence of the WOLEDs at the voltage range of 7-11 V; (d) CIE coordination (x, y) and correlated color temperature (CCT) variations of the WOLEDs at different luminance.

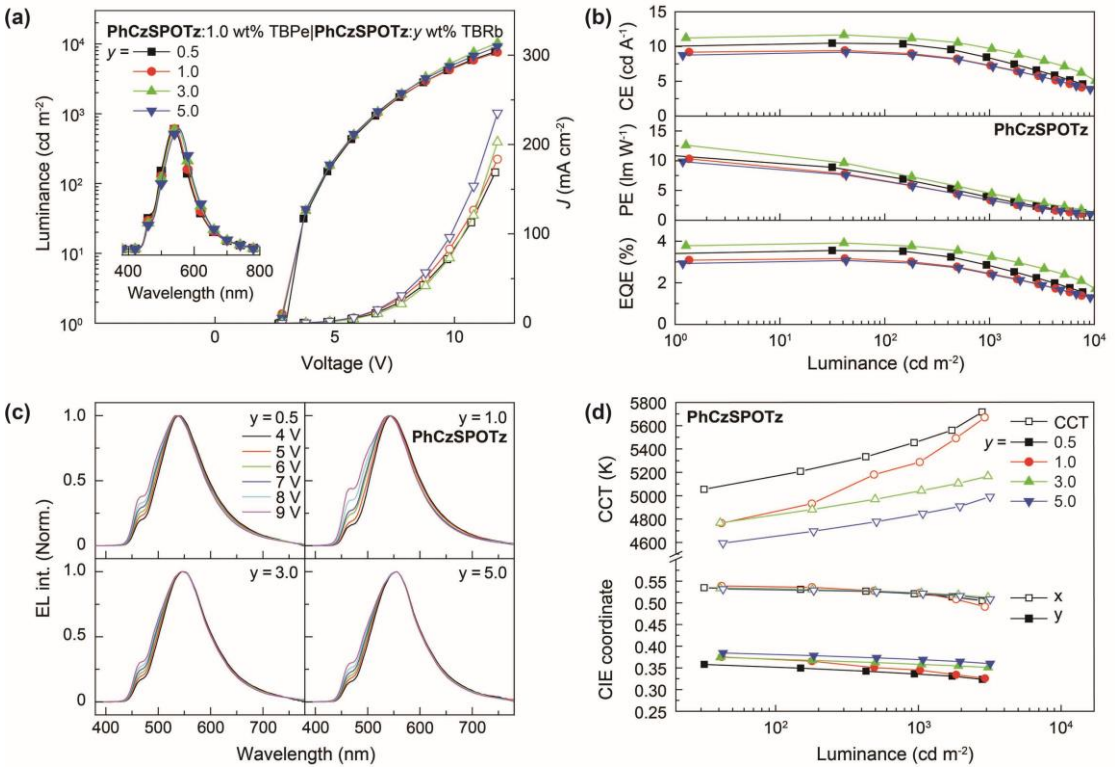

Figure S14. (a) Luminance-current density (*J*)-voltage curves and EL spectra (inset) of PhCzSPOTz:1.0 wt% TBPe|PhCzSPOTz:*y* wt% TBRb-based singly doped *d*EML WOLEDs with different TBRb concentration of 0.5, 1.0, 3.0 and 5.0 wt%; (b) efficiencies-luminance relationships of the WOLEDs; (c) EL spectrum dependence of the WOLEDs at the voltage range of 4-9 V; (d) CIE coordination (x, y) and correlated color temperature (CCT) variations of the WOLEDs at different luminance.

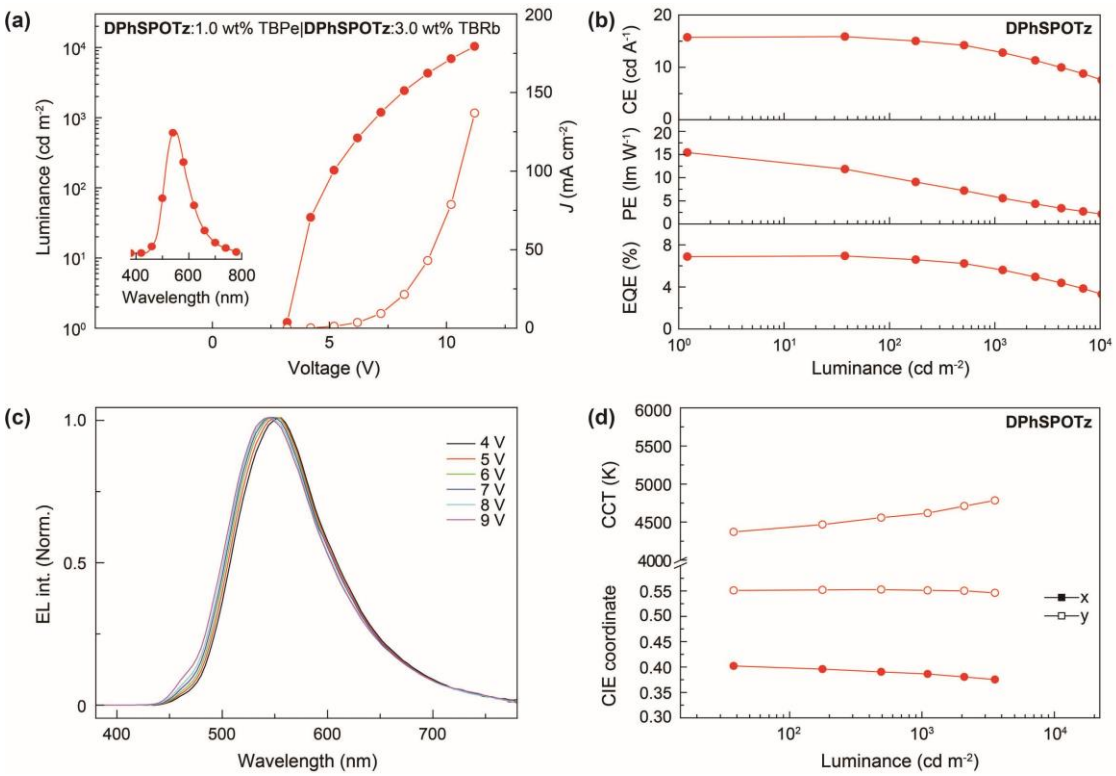

Figure S15. (a) Luminance-current density (*J*)-voltage curves and EL spectra (inset) of DPhSPOTz:1.0 wt% TBPe|DPhSPOTz:3.0 wt% TBRb-based singly doped *d*EML WOLEDs; (b) efficiencies-luminance relationships of the WOLEDs; (c) EL spectrum dependence of the WOLEDs at the voltage range of 4-9 V; (d) CIE coordination (x, y) and correlated color temperature (CCT) variations of the WOLEDs at different luminance.

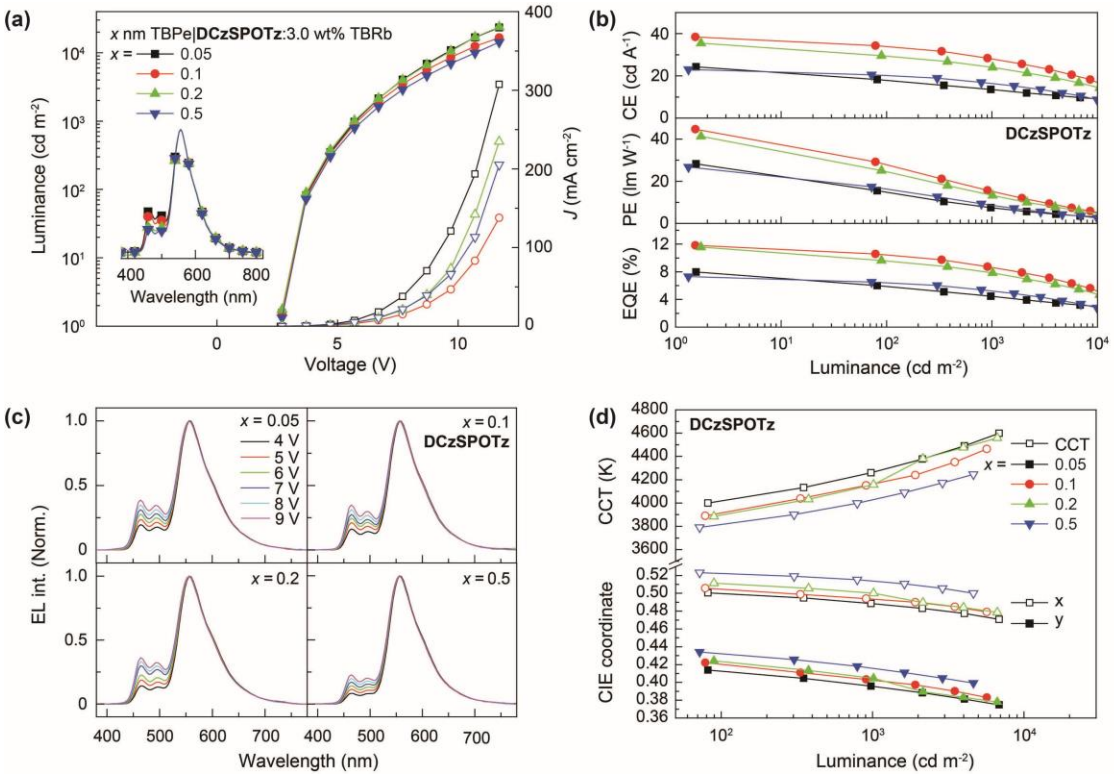

Figure S16. (a) Luminance-current density (*J*)-voltage curves and EL spectra (inset) of *x* nm TBPe|DCzSPOTz:*y* wt% TBRb-based singly doped *d*EML WOLEDs with different TBPe thicknesses of 0.05, 0.1, 0.2 and 0.5 nm; (b) efficiencies-luminance relationships of the WOLEDs; (c) EL spectrum dependence of the WOLEDs at the voltage range of 4-9 V; (d) CIE coordination (x, y) and correlated color temperature (CCT) variations of the WOLEDs at different luminance.

Considering the highest occupied molecular orbital (HOMO) of TBPe between those of hole-transporting TCTA layer and TBRb doped PO matrixes, the TBPe layer would facilitate hole injection into the latter, which remedied carrier flux unbalance in electron-transporting predominant DPhSPOTz matrix. Therefore, compared to its yellow diodes, the incorporation of 0.1 nm TBPe reduced the driving voltages of DPhSPOTz based WOLEDs, and simultaneously increased the maximum luminance. On the contrary, the incorporation of 0.1 nm TBPe layer increased the driving voltages and decreased the maximum luminance of DCzSPOTz hosted UTBL WOLEDs. While, compared to the other two PO hosts, PhCzSPOTz endowed its UTBL WOLEDs with the lowest driving voltages of 2.6, 3.5 and 4.7 V at 1, 100 and

1000 cd m^{-2}, respectively, and the largest maximum luminance beyond 60000 cd m^{-2}, which were comparable to the values of its yellow diodes.

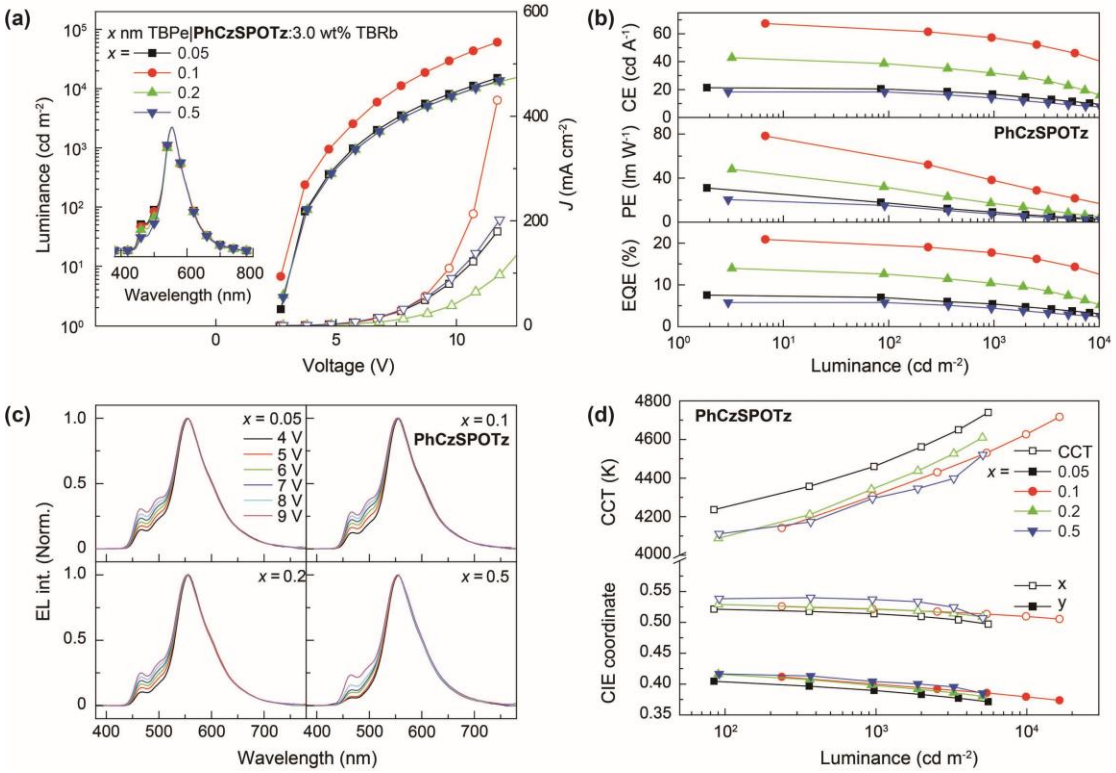

Figure S17. (a) Luminance-current density (*J*)-voltage curves and EL spectra (inset) of *x* nm TBPe|PhCzSPOTz:*y* wt% TBRb-based singly doped *d*EML WOLEDs with different TBPe thicknesses of 0.05, 0.1, 0.2 and 0.5 nm; (b) efficiencies-luminance relationships of the WOLEDs; (c) EL spectrum dependence of the WOLEDs at the voltage range of 4-9 V; (d) CIE coordination (x, y) and correlated color temperature (CCT) variations of the WOLEDs at different luminance.

It is interesting that for DCzSPOTz and PhCzSPOTz hosted UTBL WOLEDs, increasing TBPe thickness induced the decease of blue components. It means blue emissios from TBPe would be the combination of direct exciton formation on TBPe layers and FRET from PO host matrixes. The former can avert triplet leakge from PO host to TBPe, but waste triplet excitons directly formed on TBPe. For the latter, TADF-featured PO matrixes can facilitate triplet utilization, but should support sufficient singlet energy transfer to both TBPe and TBRb. In this case, decreasing

TBPe thickness would reduce direct exciton allocation to TBPe, but enhance spatial separation effect. Therefore, at x = 0.05 nm, more excitons were formed on host matrixes, and then difussed to TBPe layer, which were accompanied by triplet leakge; while, at x = 0.5 nm, more excitons were directly formed in TBPe layer, rendering the largest relative intensities of blue emissions. But, more triplet excitons were simultaneously wasted by TBPe. It is showed that the direct exciton allocation and singlet FRET to TBPe were balanced at x = 0.1 nm, rendering the highest efficiencies and reduced roll-offs.

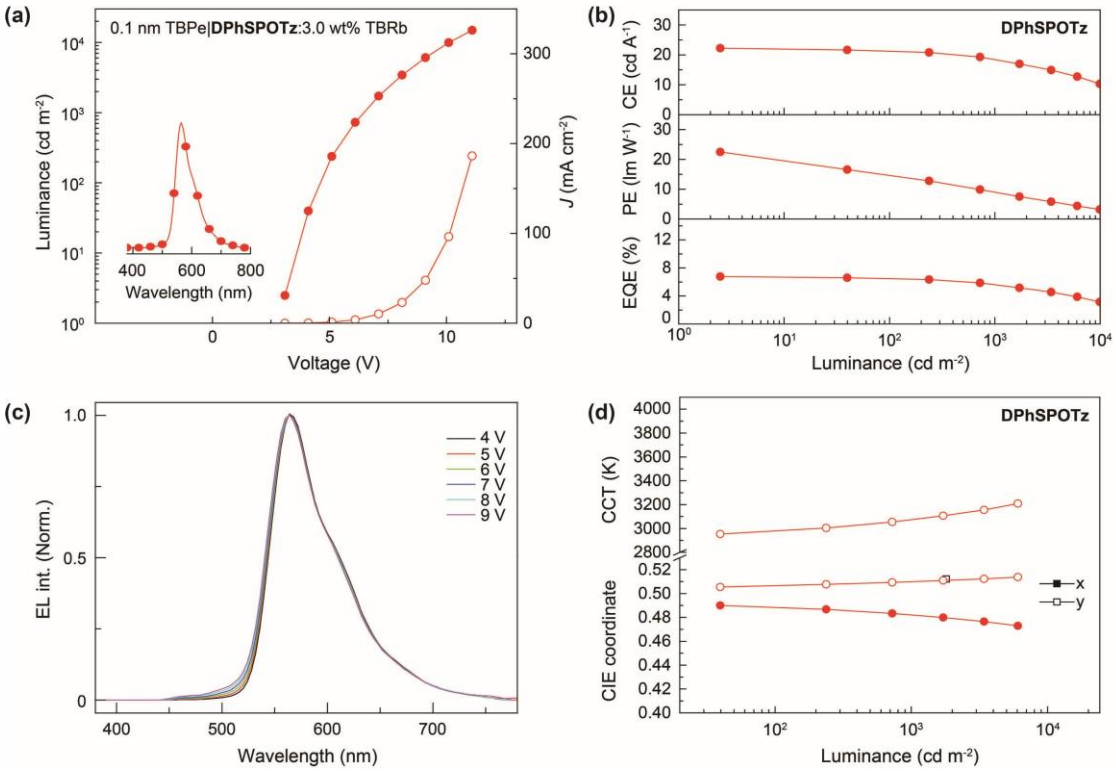

Figure S18. (a) Luminance-current density (*J*)-voltage curves and EL spectra (inset) of 0.1 nm TBPe|DPhSPOTz:3.0 wt% TBRb-based singly doped *d*EML WOLEDs; (b) efficiencies-luminance relationships of the WOLEDs; (c) EL spectrum dependence of the WOLEDs at the voltage range of 4-9 V; (d) CIE coordination (x, y) and correlated color temperature (CCT) variations of the WOLEDs at different luminance.

It is showed that along with driving voltage increasing, intensities of blue components in EL spectra of WOLEDs were also gradually enhanced, indicating recombination zone shift to anode due to facilitated electron injection and transport. Nevertheless, CCT values of DCzSPOTz and PhCzSPOTz based WOLEDs were around 4000 K, with variation less than 800 K, corresponding to warm-white emissions.

Table S2. EL performance of OLEDs using DCzSPOTz, PhCzSPOTz and DPhSPOTz as hosts.

Device	Emitter	$V^{[a]}$ (V)	$L_{max}^{[b]}$ (cd m^{-2})	$\eta^{[c]}$			CIE (x, y)
				η_{CE} (cd A^{-1})	η_{PE} (lm W^{-1})	η_{EQE} (%)	
Blue	DCzSPOTz	3.3, 6.5, 9.7	2523	1.1, 1.1, 1.0	1.1, 0.5, 0.3	0.5, 0.5, 0.4	0.19, 0.33
	PhCzSPOTz	2.9, 4.8, 7.7	4490	4.8, 4.8, 3.7	4.3, 3.1, 1.5	1.7, 1.7, 1.3	0.37, 0.53
	DPhSPOTz	3.2, 4.6, 6.8	3848	8.5, 8.0, 5.6	8.1, 5.6, 2.6	2.7, 2.6, 1.8	0.38, 0.56
Yellow	DCzSPOTz	2.6, 3.7, 5.2	45405	61.3, 58.4, 51.9	74.0, 50.5, 31.5	18.7, 17.7, 15.8	0.51, 0.49
	PhCzSPOTz	2.6, 3.5, 5.0	59267	66.0, 64.1, 60.6	78.3, 58.7, 38.8	20.9, 20.3, 19.2	0.50, 0.50
	DPhSPOTz	3.6, 5.3, 7.8	11096	20.5, 20.0, 18.3	15.6, 12.1, 7.3	6.4, 6.3, 5.7	0.50, 0.50
*s*EML WOLED	DCzSPOTz	2.9, 4.5, 6.7	23850	13.6, 13.5, 12.4	14.6, 9.6, 5.8	4.2, 4.1, 3.8	0.48, 0.51
	PhCzSPOTz	2.7, 3.9, 6.1	15130	16.4, 16.3, 14.5	17.8, 13.0, 7.4	6.0, 5.9, 4.4	0.48, 0.51
	DPhSPOTz	3.0, 4.2, 6.0	11280	10.9, 10.6, 9.0	11.4, 8.0, 4.7	2.9, 2.8, 2.4	0.48, 0.51
*d*EML WOLED	DCzSPOTz	3.0, 5.2, 7.7	8029	3.2, 3.2, 3.2	3.0, 2.0, 1.3	1.2, 1.2, 1.2	0.33, 0.41
	PhCzSPOTz	2.8, 4.4, 6.7	10270	11.7, 11.4, 9.9	12.6, 8.3, 4.6	3.9, 3.8, 3.3	0.36, 0.52
	DPhSPOTz	3.2, 4.8, 7.0	10350	15.9, 15.3, 13.13	15.4, 10.0, 5.9	7.0, 6.7, 5.8	0.39, 0.55
UTBL WOLED	DCzSPOTz	2.7, 3.9, 5.8	16580	38.5, 34.0, 28.1	44.7, 28.4, 15.4	11.8, 10.4, 8.8	0.40, 0.49
	PhCzSPOTz	2.6, 3.5, 4.7	60680	67.3, 62.9, 57.0	78.3, 58.4, 38.0	20.9, 19.4, 17.7	0.40, 0.52
	DPhSPOTz	3.1, 4.6, 6.5	14920	22.2, 21.2, 18.3	22.5, 14.4, 8.9	6.8, 6.5, 5.5	0.48, 0.51

[a] At 1, 100 and 1000 cd m^{-2}; [b] the maximum luminance; [c] EL efficiencies at the maximum and 100 and 1000 cd m^{-2}.

VI. Gaussian Simulation Results (Fig. S19)

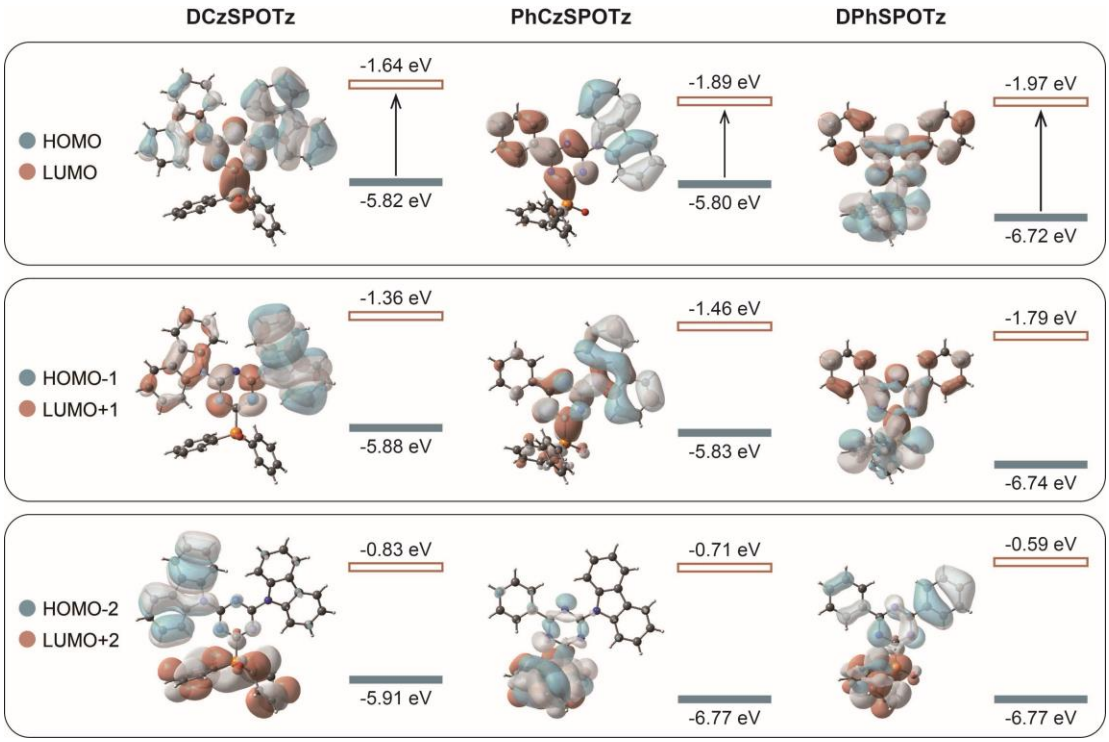

Figure S19. Electron-cloud distribution contours and energy levels of the HOMOs and LUMOs of DCzSPOTz, PhCzSPOTz and DPhSPOTz, simulated according to single-crystal structures.

For the $S_0 \rightarrow S_1$ excitation, in contrast to frontier molecular orbitals (FMO) of the first singlet locally-excited state (^{1}LE) overlapped on diphenyltriazine of DPhSPOTz, "hole" and "particle" of DCzSPOTz monomer are mainly distributed on Cz and Tz groups, respectively, corresponding to the typical charge-transfer-featured S_1 state (^{1}CT) (**Figure 3a**). However, it is noted that due to the limited conjugation of Tz in DCzSPOTz, its "hole" and "particle" are still considerably overlapped on Tz and pyrrole of Cz groups, which is similar to the situation of its HOMO and lowest unoccupied molecular orbitals (LUMO) (**Figure S19**). In comparison, "particle" of the singlet excitation is extended to phenyl linked with Tz of PhCzSPOTz; meanwhile, despite similar ^{1}CT-featured state, the singlet "hole"-"particle" overlap of

PhCzSPOTz is limited on Tz core, giving rise to the elongated “hole”-“particle” distance ($d_{H\text{-}L}$) (**Figure 3b**). The stronger ICT effect of PhCzSPOTz leads to its lowest calculated S_1 energy level of 3.36 eV, compared to 3.58 and 3.81 eV for DCzSPOTz and DPhSPOTz, which is in accord to optical results. According to the $S_0 \rightarrow T_1$ excitation, all the PO molecules exhibit the locally-excited predominant T_1 states (^{3}LE) with large “hole”-“particle” overlaps on Cz group or diphenyltriazine, rendering their almost identical T_1 energy levels of ~3.15 eV. Consequently, PhCzSPOTz with the smallest single-molecular ΔE_{ST} value of 0.26 eV would be superior in RISC, in comparison to DCzSPOTz and DPhSPOTz with ΔE_{ST} values of 0.43 and 0.67 eV, respectively.

VII. Photophyscial Analysis Results (Figs S20-S26 and Table S3)

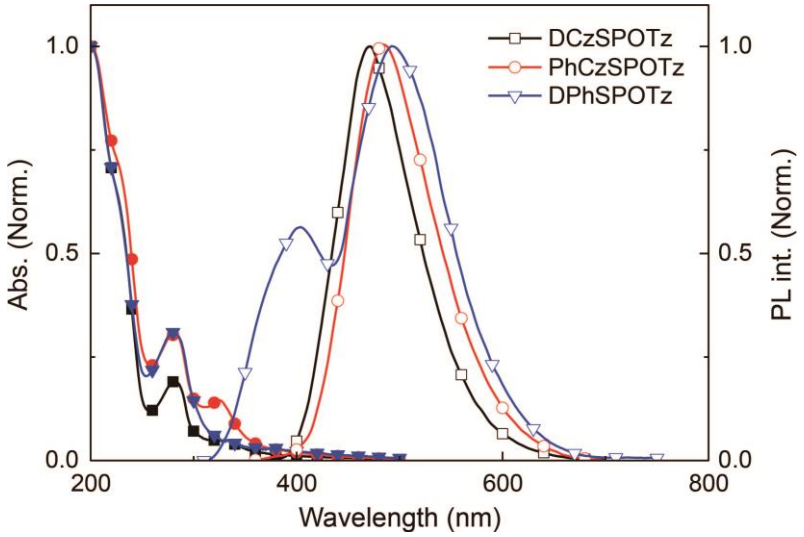

Figure S20. Absorption and photoluminescence (PL) spectra of *vacuum*-evaporated neat DCzSPOTz, PhCzSPOTz and DPhSPOTz films.

Electronic absorption spectra of neat DCzSPOTz and PhCzSPOTz films show the fine structures similar to the spectra in dilute solutions, reflecting the limited intermolecular interactions (**Figure S20**). In contrast, neat DPhSPOTz film displays an additional absorption tail in the range of 300-400 nm. Due to its monopolar characteristics, neat DPhSPOTz film shows an unchanged molecular emission peak at 404 nm, which is in accord to 406 nm in solutions, but the main peak at 494 nm corresponds to excimer emission with a bathochromic shift of 60 nm.

Delayed fluorescence (DF) proportion in emission of neat PhCzSPOTz film is the biggest among these PO hosts, owing to its smallest ΔE_{ST}. Despite weaker than DCzSPOTz film, DPhSPOTz film reveals a DF component at ~490 nm, consistent to its excimer emission.

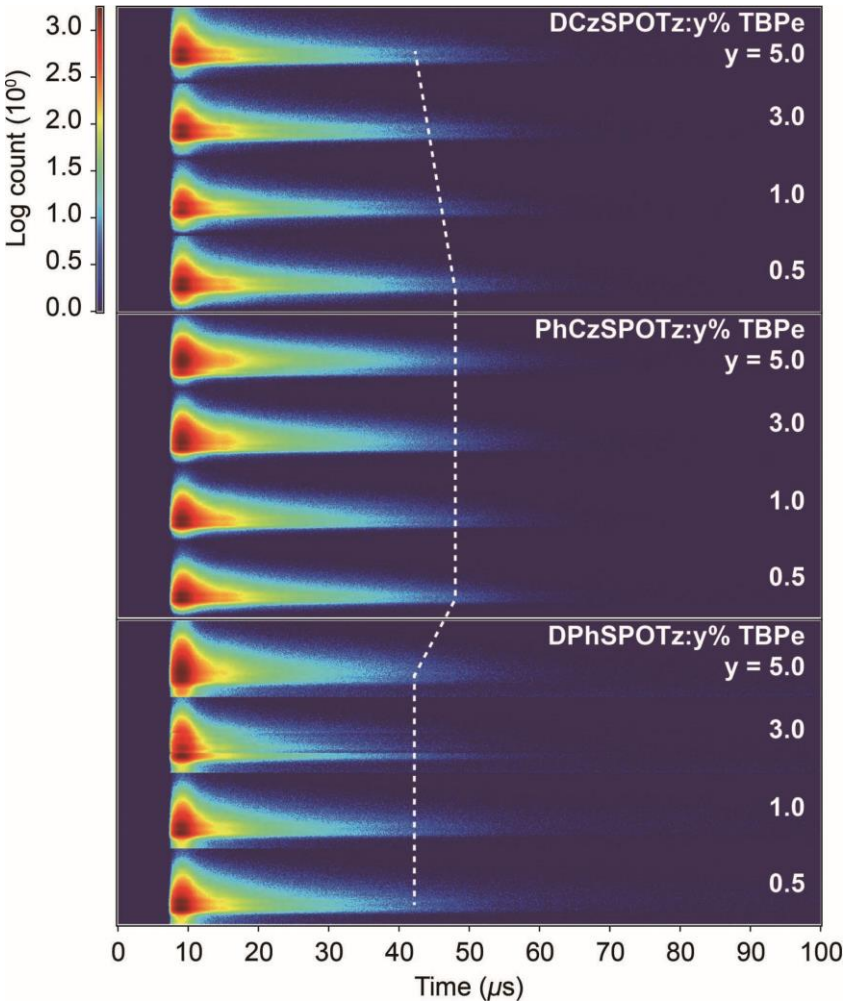

Figure S21. Transient emission contours of *vacuum*-evaporated blue-emitting host:y% TBPe films, in which hosts are DCzSPOTz, PhCzSPOTz and DPhSPOTz, respectively, and x = 0.5-5.

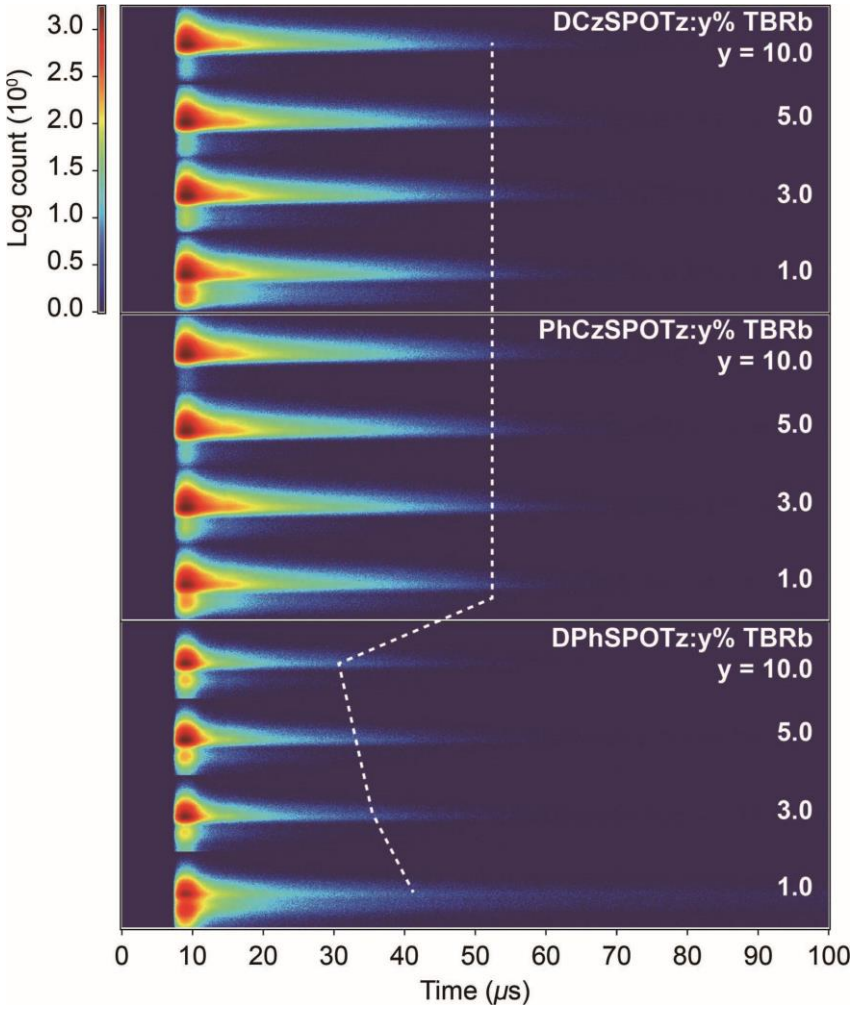

Figure S22. Transient emission contours of *vacuum*-evaporated yellow-emitting host:y% TBRb films, in which hosts are DCzSPOTz, PhCzSPOTz and DPhSPOTz, respectively, and y = 1.0-10.

For PhCzSPOTz and DPhSPOTz, DF components are basically remained after TBRb doping; while, DF proportion of DCzSPOTz hosted film is even increased, due to more facile exciton migration in DCzSPOTz matrix.

Since yellow diodes only displayed pure TBRb-originated emissions, direct carrier capture and recombination by TBRb should make significant contributions to EL processes.

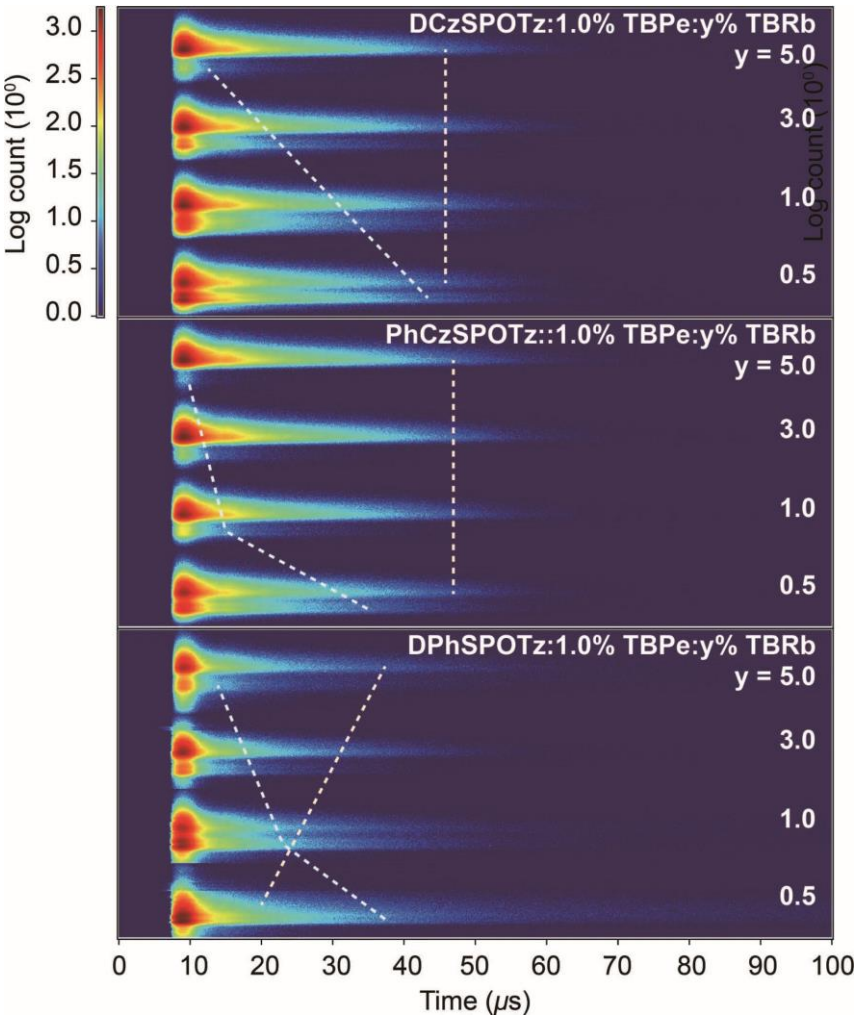

Figure S23. Transient emission contours of *vacuum*-evaporated dually doped single-layer host:1.0% TPBe:y% TBRb films, in which hosts are DCzSPOTz, PhCzSPOTz and DPhSPOTz, respectively, and y = 0.5-5.0.

Blue intensity in PL spectrum of DPhSPOTz:1% TBPe:3% TBRb film is stronger than its EL spectrum, because of direct carrier and exciton capture by TBRb in monopolar DPhSPOTz matrix of devices.

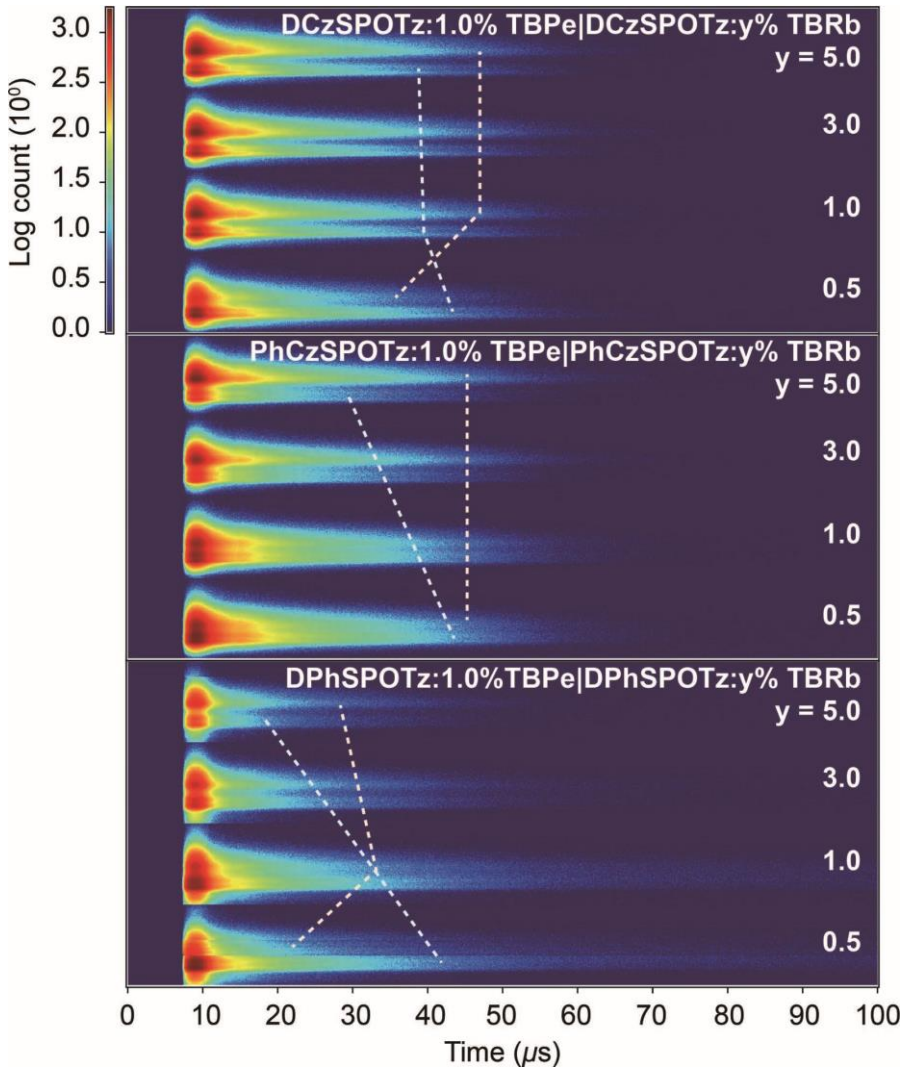

Figure S24. Transient emission contours of *vacuum*-evaporated singly doped dual-layer host:1.0% TPBe|host:y% TBRb films, in which hosts are DCzSPOTz, PhCzSPOTz and DPhSPOTz, respectively, and y = 0.5-5.0.

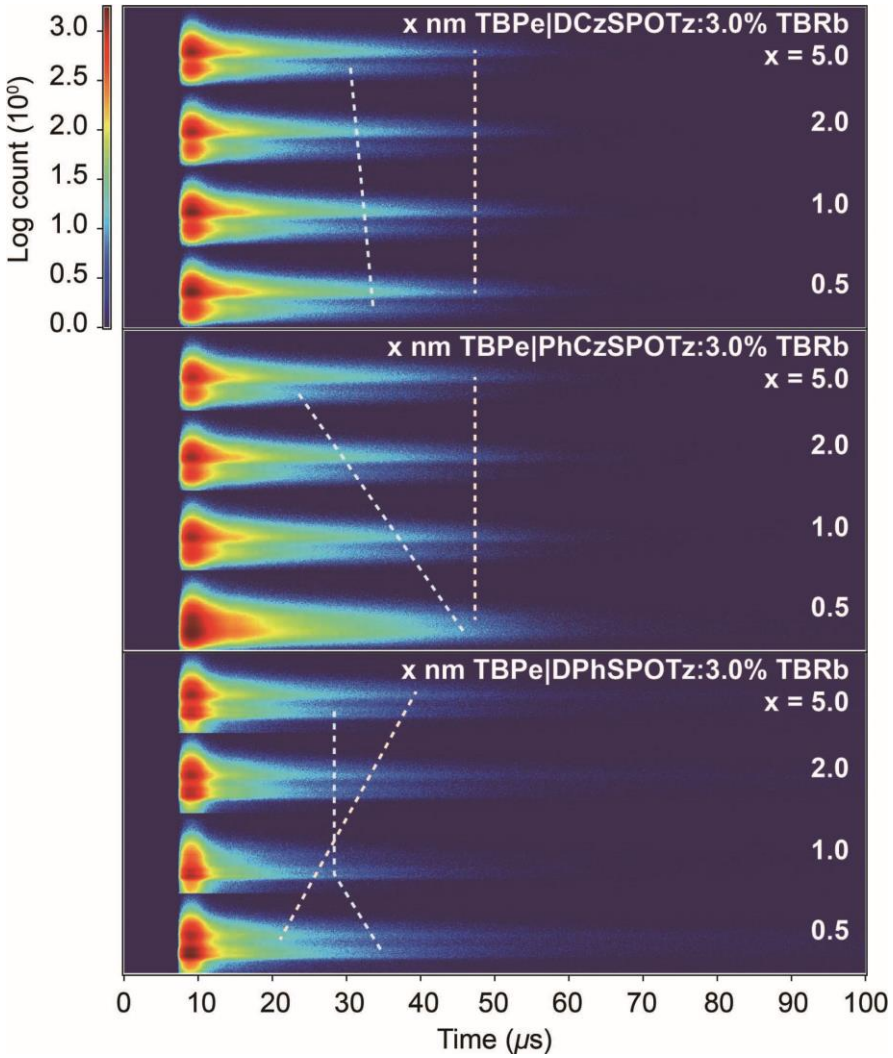

Figure S25. Transient emission contours of *vacuum*-evaporated quasi-dual-layer x nm TPBe:y% TBRb films, in which hosts are DCzSPOTz, PhCzSPOTz and DPhSPOTz, respectively, and x = 0.5-5.0 nm.

PL spectrum of DPhSPOTz hosted UTBL film is identical to its *d*EML film, indicating the similar predominance of TBPe in energy transfer. However, spatial separation of DCzSPOTz and TBPe decreases blue intensity. On the contrary, blue component from PhCzSPOTz hosted UTBL film is largely enhanced, owing to the combined quenching suppression and energy transfer preservation.

However, the situation of DCzSPOTz hosted *d*EML and UTBL films is opposite. Since higher extinction coefficient of TBPe than that of DCzTzSPO matrix, excitation

energy is mainly absorbed by singlet-harvesting-only TBPe at incident side, leading to PF predominance and DF reduction.

Due to the competition in exciton allocation, all the quantum efficiencies (η), including η_{PL}, efficiencies of PF (η_{PF}), DF (η_{DF}), RISC (η_{RISC}) and exciton utilization in the corresponding diodes (η_{EUE}), and transition rate constants (k) of PF (k_{PF}), DF (k_{DF}), RISC (k_{RISC}), singlet radiation (k_r^S) and singlet (k_{nr}^S) and triplet (k_{nr}^T) nonradiation of blue components from DPhSPOTz hosted white films are nearly equal, but reduced in comparison to its singly doped blue film (**Figure 4e**). However, for yellow components of DPhSPOTz hosted white films, the efficiencies and rate constants of TADF transitions firstly decrease for *s*EML film, and then gradually increase for *d*EML and UTBL films, indicating the effectiveness of the latter in alleviating dopant-dopant quenching. On the contrary, for PhCzSPOTz and DCzSPOTz hosted *s*EML, *d*EML and UTBL films, the radiative efficiencies (η_{PL}, η_{PF}, η_{DF} and η_{EUE}) and rate constants (k_{PF}, k_{DF} and k_{RISC}) of both blue and yellow components sharply decrease, and then markedly increase. The difference is that *s*EML and *d*EML films respectively reveal the lowest η and k values of blue and yellow components, revealing the most serious quenching of TBPe by direct interactions with high-concentration TBRb in *s*EMLs, and the doubled triplet quenching and locale and deficient exciton allocation in *d*EMLs. Meanwhile, the nearly identical transition properties of DPhSPOTz based *d*EML and UTBL films reflect the comparable spatial effect on restraining dopant-dopant quenching.

VIII. Electrochemical Analysis (Fig. S26)

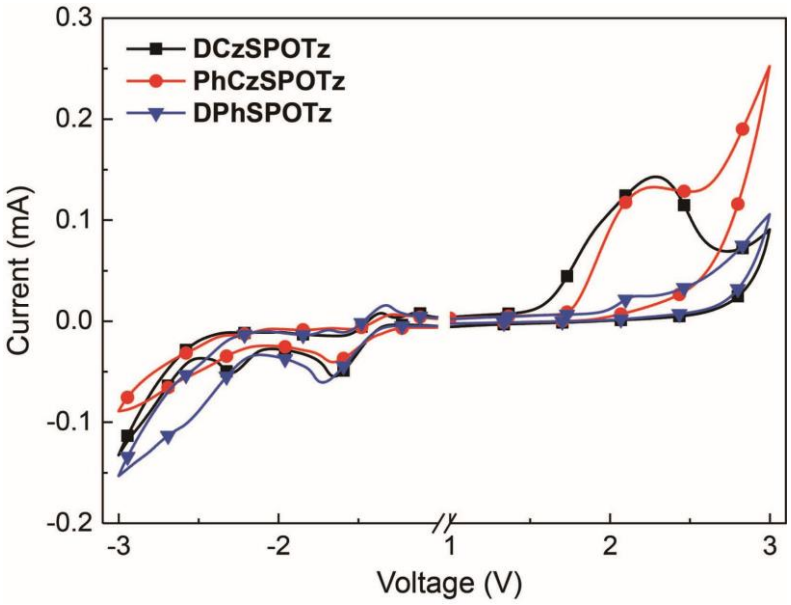

Figure S26. Cyclic voltammogram of **DCzSPOTz**, **PhCzSPOTz** and **DPhSPOTz** measured at room temperature with the scanning rate of 100 mV s^{-1}.

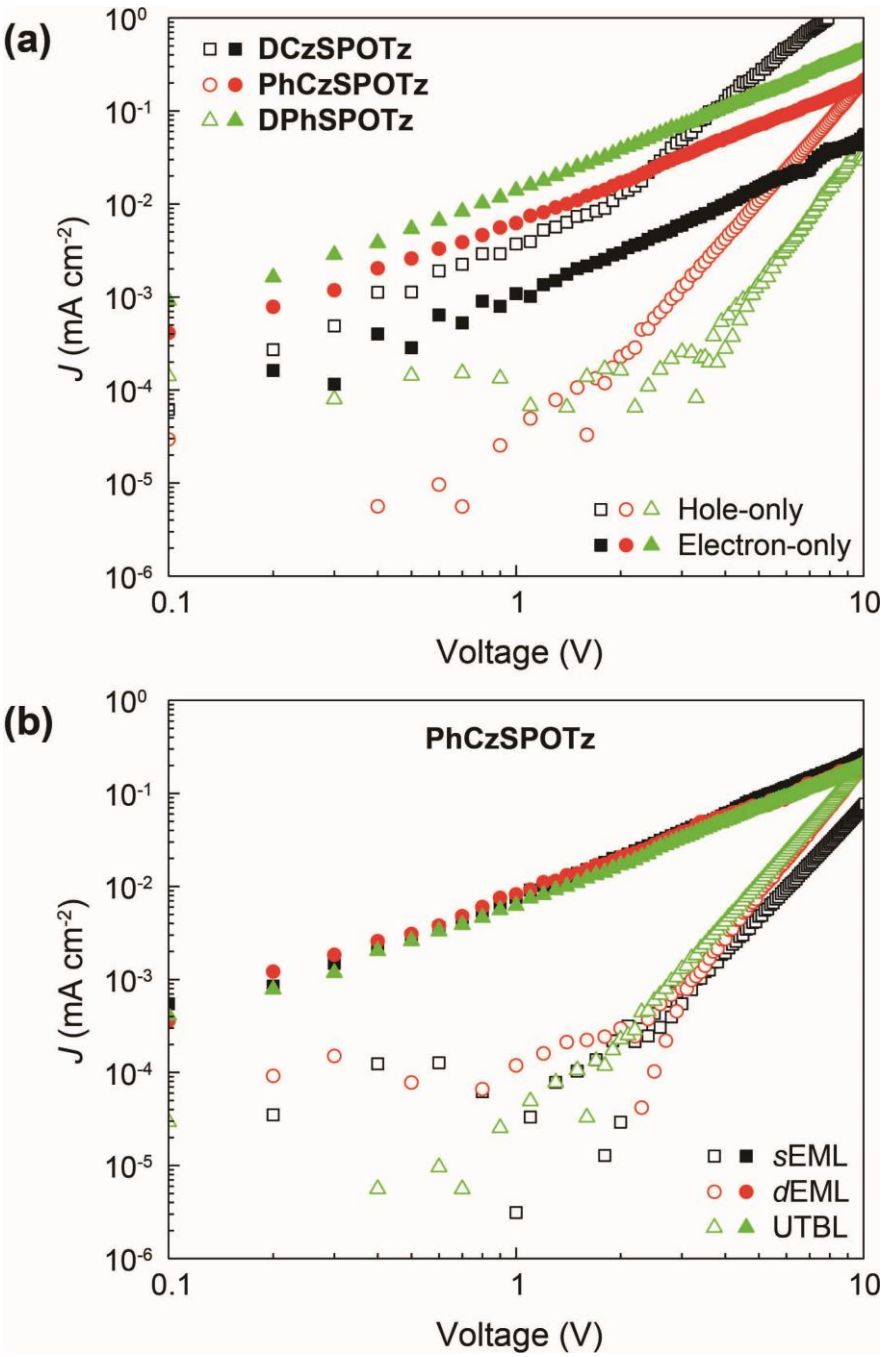

Figure S27. IV characteristics of single-carrier-transporting devices based on **DCzSPOTz**, **PhCzSPOTz** and **DPhSPOTz**. (**a**) Voltage-current density (*J*) curves of single-carrier-transporting devices with semi-UTBL configurations of ITO|MoO_3 (6 nm)|TAPC (40 nm)|TCTA (10 nm)|TBPe (0.1 nm)|host:3% TBRb (15 nm)|TBPe (0.1 nm)|TCTA (10 nm)|TAPC (40 nm)|MoO_3 (6 nm)|Al (100 nm) and ITO|LiF (1 nm)|DBTDPO (40 nm)|TBPe (0.1 nm)|host:3% TBRb (15 nm)|TBPe (0.1 nm)|DBTDPO (40 nm)|LiF (1 nm)|Al (100 nm), respectively; (**b**) Voltage-current

density (*J*) curves of single-carrier-transporting devices based on PhCzSPOTz with *s*EML, *d*EML and semi-UTBL configurations. *s*EML and *d*EML-type configuration of ITO|MoO_3 (6 nm)|TAPC (40 nm)|TCTA (10 nm)|EMLs (15 nm)|TCTA (10 nm)|TAPC (40 nm)|MoO_3 (6 nm)|Al (100 nm) and ITO|LiF (1 nm)|DBTDPO (40 nm)|EMLs (15 nm)|DBTDPO (40 nm)|LiF (1 nm)|Al (100 nm), respectively.

Table S3. Transition parameters of DCzSPOTz, PhCzSPOTz and DPhSPOTz based films.

TADF host	Emission color	η_{PL}[a] (%)	τ_{PF}[b] (ns)	τ_{DF}[c] (μs)	η_{PF}[d] (%)	η_{DF}[e] (%)	k_{PF}[f] (10^7 s^{-1})	k_{DF}[g] (10^4 s^{-1})	k_{ISC}[h] (10^6 s^{-1})	k_{RISC}[i] (10^4 s^{-1})	k_r^S[j] (10^6 s^{-1})	k_{nr}^S[k] (10^6 s^{-1})	k_{nr}^T[l] (10^4 s^{-1})	η_{ISC}[m] (%)	η_{RISC}[n] (%)
Pure host films															
DCzSPOTz	-	25	6.5	8.4	13	12	2.00	1.43	9.60	2.75	2.60	7.80	1.07	48	72
PhCzSPOTz		28	15.4	12.4	11.6	16.4	0.75	1.32	4.41	3.19	0.87	2.25	0.95	59	77
DPhSPOTz		3.6	41.8	11.2	2	1.6	0.05	0.14	0.21	0.26	0.01	0.26	0.14	44	65
Host:1% TPBe (Blue films)															
DCzSPOTz	**Blue**	13.7	7.4	12.3	6.9	6.8	0.93	0.55	4.63	1.10	0.64	4.05	0.48	50	70
PhCzSPOTz		26.4	16.3	14.4	13.6	12.8	0.83	0.89	4.05	1.73	1.13	3.16	0.65	48	73
DPhSPOTz		36.2	13.7	9.1	20.4	15.8	1.49	1.74	6.50	3.08	3.04	5.35	1.11	44	74
Host:3% TBRb (Yellow films)															
DCzSPOTz	**Yellow**	90.9	14.3	13.5	46.2	44.7	3.23	3.31	15.89	6.51	14.93	1.49	0.30	49	96
PhCzSPOTz		99.0	13.4	14.1	45	54	3.36	3.83	18.32	8.43	15.11	0.15	0.04	55	**100**
DPhSPOTz		26.3	16.3	5.7	23.2	3.1	1.42	0.54	1.68	0.62	3.30	9.25	0.40	12	61
Host:1% TPBe:3%TBRb (sEML white films)															
DCzSPOTz	**Blue**	1.5	2.5	11.1	0.7	0.8	0.28	0.07	1.49	0.15	0.02	1.29	0.07	53	69
PhCzSPOTz		0.6	4.3	11.3	0.3	0.3	0.07	0.03	0.35	0.05	0.00	0.35	0.03	50	67
DPhSPOTz		2.3	5.3	5.3	1.5	0.8	0.28	0.15	0.98	0.23	0.04	1.80	0.15	35	61
DCzSPOTz	**Yellow**	32.5	16.7	11.5	17.5	15.0	1.05	1.30	4.84	2.42	1.83	3.81	0.88	46	73
PhCzSPOTz		53.1	15.3	14.4	24.2	28.9	1.58	2.01	8.61	4.40	3.83	3.38	0.94	54	82
DPhSPOTz		11.5	16.5	5.5	7.4	4.1	0.45	0.75	1.60	1.16	0.33	2.55	0.66	36	64
Host:1% TPBe|Host:3%TBRb															
DCzSPOTz	**Blue**	2.6	7.3	14.9	1.3	1.3	0.18	0.09	0.89	0.17	0.02	0.87	0.08	50	67

PhCzSPOTz		2.5	15.3	16.6	1.1	1.4	0.07	0.08	0.40	0.19	0.01	0.31	0.08	56	70
DPhSPOTz		3.2	5.8	8.1	2.0	1.2	0.34	0.15	1.29	0.24	0.07	2.09	0.14	38	62
DCzSPOTz		5.3	14.7	14.2	2.1	3.2	0.14	0.23	0.86	0.57	0.03	0.54	0.21	60	73
PhCzSPOTz	**Yellow**	20.3	14.2	14.4	10.8	9.5	0.76	0.66	3.56	1.24	0.82	3.22	0.53	47	70
DPhSPOTz		38.5	16.7	10.7	20.9	17.6	1.25	1.64	5.72	3.03	2.62	4.18	1.01	46	75
1 nm TPBe|Host:3%TBRb															
DCzSPOTz		6.2	5	12.3	2.8	3.4	0.56	0.28	3.07	0.61	0.16	2.37	0.26	55	70
PhCzSPOTz	**Blue**	12.3	12	14.2	7.2	5.1	0.60	0.36	2.49	0.61	0.43	3.08	0.31	41	66
DPhSPOTz		2.1	5.2	10.7	1.3	0.8	0.25	0.07	0.95	0.12	0.03	1.52	0.07	38	62
DCzSPOTz		64.5	15.3	12.3	30.7	33.8	2.01	2.75	10.51	5.77	6.16	3.39	0.98	52	86
PhCzSPOTz	**Yellow**	86.9	19.8	14.3	36.8	50.1	1.86	3.50	10.72	8.27	6.84	1.03	0.46	58	**95**
DPhSPOTz		38	19.2	9.3	25.0	13.0	1.30	1.40	4.45	2.12	3.26	5.31	0.87	34	71

[a] Absolute PL quantum yield measured with integrating spheres; Lifetime of [b] prompt fluorescence (PF) and [c] delayed fluorescence (DF) ; Quantum efficiency of [d] PF and [e] DF; Rate constants of [f] PF, [g] DF, [h] intersystem crossing (ISC), [i] reverse intersystem crossing (RISC), [j] singlet radiation and [k] nonradiation, and [l] triplet nonradiation; [m] ISC efficiency; [n] RISC efficiency. For DPhSPOTz, RISC and DF related parameters corresponds to DPhSPOTz excimer based process.

IX. EL Kinetics (Figs S27-S31)

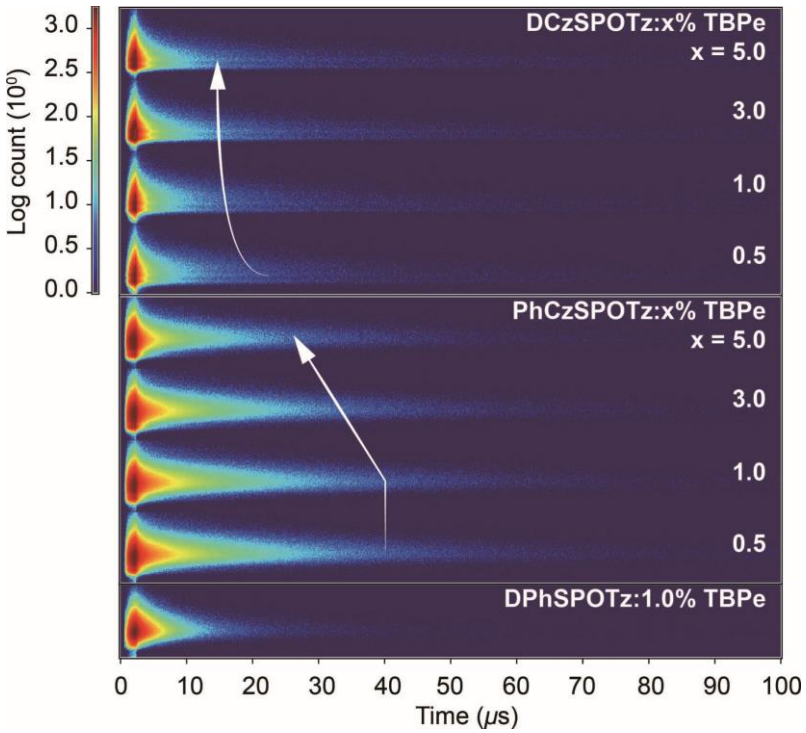

Figure S28. Time resolved EL emission contours of host:x% TBPe-based blue-emitting diodes.

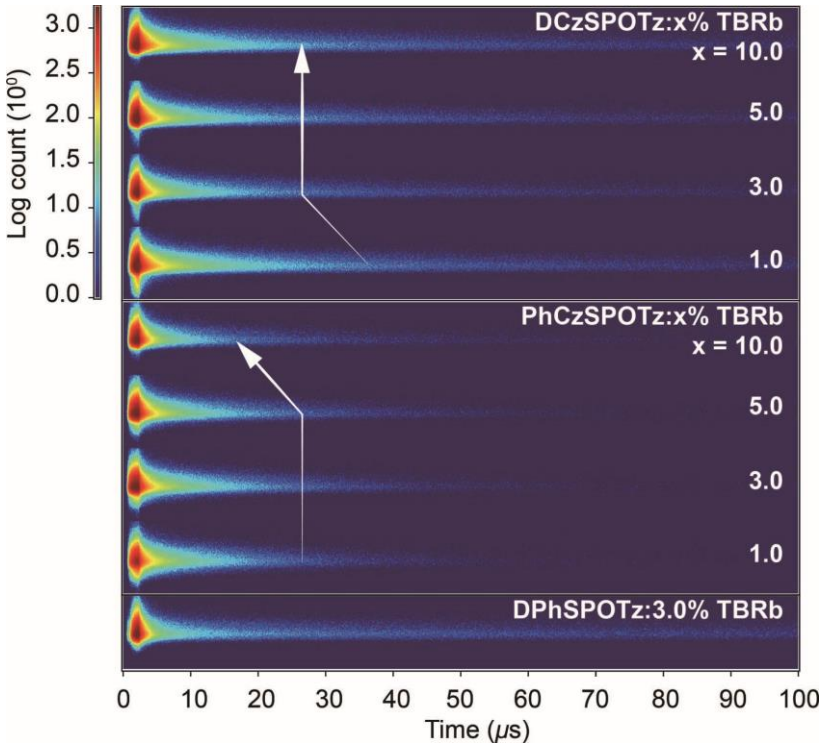

Figure S29. Time resolved EL emission contours of host:x% TBRb-based yellow-emitting diodes.

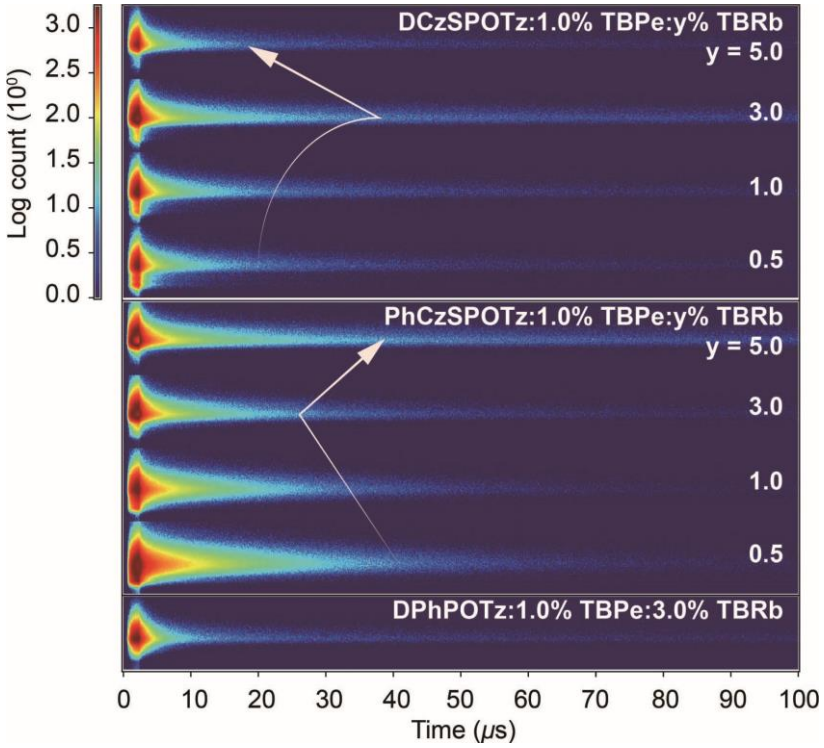

Figure S30. Time resolved EL emission contours of host:1% TBPe:y% TBRb-based *s*EML WOLEDs.

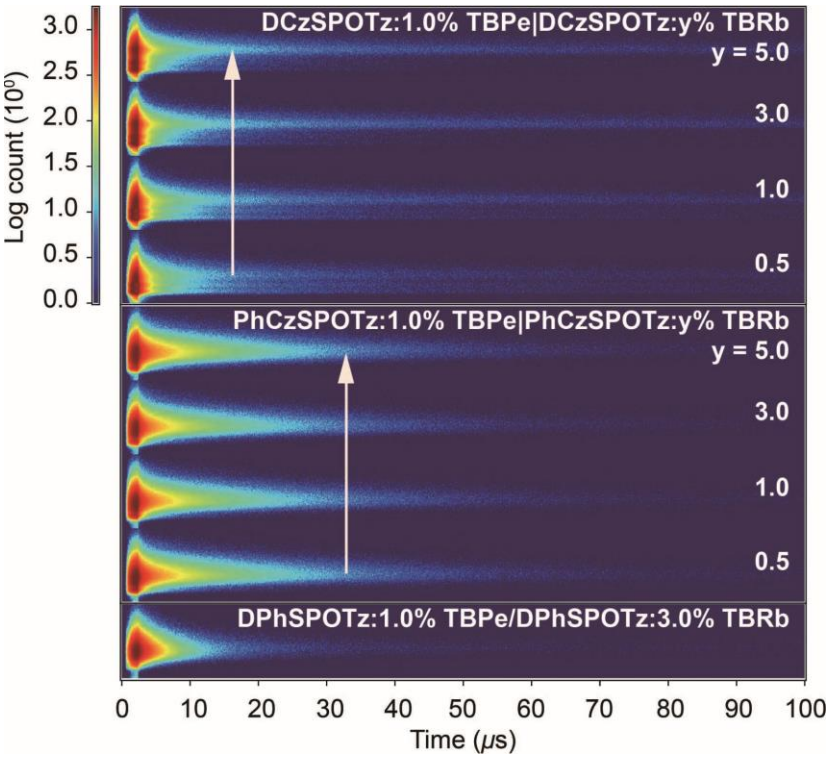

Figure S31. Time resolved EL emission contours of host:1% TBPe|host:y% TBRb-based *d*EML WOLEDs.

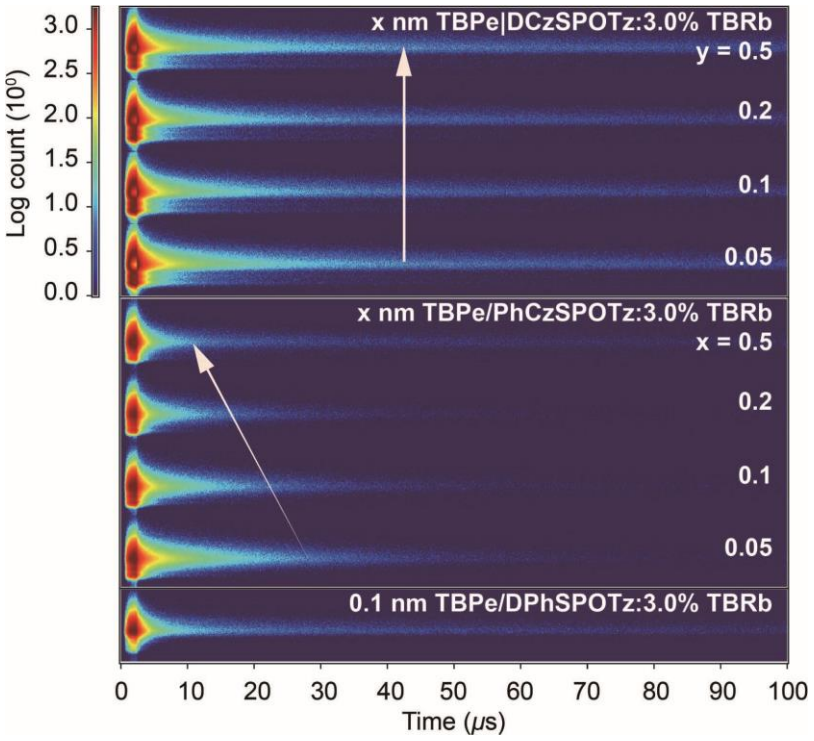

Figure S32. Time resolved EL emission contours of *x* nm TBPe|host:3.0% TBRb-based UTBL WOLEDs.

X. References

[1] A. D. Becke, J. Chem. Phys. 1993, 98, 5648.
[2] C. Lee, W. Yang, R. G. Parr, Phys. Rev. B 1988, 37, 785.
[3] R. L. Martin, J. Chem. Phys. 2003, 118, 4775.
[4] M. J. Frisch, G. W. Trucks, H. B. Schlegel, G. E. Scuseria, M. A. Robb, J. R. Cheeseman, G. Scalmani, V. Barone, B. Mennucci, G. A. Petersson, H. Nakatsuji, M. Caricato, X. Li, H. P. Hratchian, A. F. Izmaylov, J. Bloino, G. Zheng, J. L. Sonnenberg, M. Hada, M. Ehara, K. Toyota, R. Fukuda, J. Hasegawa, M. Ishida, T. Nakajima, Y. Honda, O. Kitao, H. Nakai, T. Vreven, J. A. Montgomery, J. E. Peralta, F. Ogliaro, M. Bearpark, J. J. Heyd, E. Brothers, K. N. Kudin, V. N. Staroverov, R. Kobayashi, J. Normand, K. Raghavachari, A. Rendell, J. C. Burant, S. S. Iyengar, J. Tomasi, M. Cossi, N. Rega, J. M. Millam, M. Klene, J. E. Knox, J. B. Cross, V. Bakken, C. Adamo, J. Jaramillo, R. Gomperts, R. E. Stratmann, O. Yazyev, A. J. Austin, R. Cammi, C. Pomelli, J. W. Ochterski, R. L. Martin, K. Morokuma, V. G. Zakrzewski, G. A. Voth, P. Salvador, J. J. Dannenberg, S. Dapprich, A. D. Daniels, Ö. Farkas, J. B. Foresman, J. V. Ortiz, J. Cioslowski, D. J. Fox, Gaussian, Inc., Wallingford CT, USA, 2009.